C.1

HYDRODYNAMICS OF LASER ACCELERATED FOILS

by

GARY M. JOSIN

A THESIS SUBMITTED IN PARTIAL FULFILLMENT OF

THE REQUIREMENTS FOR THE DEGREE OF

MASTER OF SCIENCE

in

THE FACULTY OF SCIENCE

Department of Physics

We accept this major paper as conforming

to the required standard:

THE UNIVERSITY OF BRITISH COLUMBIA

September 1982

© Gary M. Josin

In presenting this thesis in partial fulfilment of the requirements for an advanced degree at the University of British Columbia, I agree that the Library shall make it freely available for reference and study. I further agree that permission for extensive copying of this thesis for scholarly purposes may be granted by the head of my department or by his or her representatives. It is understood that copying or publication of this thesis for financial gain shall not be allowed without my written permission.

Department of Physics

The University of British Columbia
1956 Main Mall
Vancouver, Canada
V6T 1Y3

Date Sept 14

ABSTRACT

A ruby laser system has been constructed and characterized to check the applicability of a diagnostic method which extracts all the hydrodynamic parameters without any knowledge of the microscopic physics. Our diagnostic method is not yet employable since strong shock waves are not generated with the available laser system. However the experimental results agree with a general heat wave model which is based on a universal heating characteristic. Furthermore the experimental results are consistent with the well documented Medusa hydrocode. It is of interest that for laser plasmas a universal heating characteristic exists from which the exhaust temperature for the laser plasma can be predicted from the laser intensity alone.

TABLE OF CONTENTS

LIST OF FIGURES

LIST OF TABLES

ACKNOWLEDGEMENTS

I would like to thank Boye Ahlborn for his enthusiasium throughout the course of this thesis and more importantly for giving me something more than a ticket for the job market. I would like to express my gratitude for the visits to the Plasma Physics division of N.R.C. Ottawa.

I would like to thank Andrew Ng for many helpful discussions and for the use of the target chamber. I would also like to thank two other members of the Plasma Physics group for their help. Hubert Houtman for helping construct the ruby laser and Allan Cheuck for rebuilding the streak unit and for troubleshoooting many electronic problems.

TO

PATTI
AND
MICHAEL

CHAPTER I

Introduction

One of the aims of a modern technological society is to develop an inexhaustible source of available energy. A recent scheme is to compress solid deuterium tritium to very high densities with a laser proir to ignition(i.e.,laser fusion).

The deuterium tritium pellet is enclosed within a higher density spherical shell. This outer shell acts like a piston or pusher when it is set in motion by the high pressure created by the absorption of the laser light and compresses the fuel to thermonuclear conditions. To study the hydrodynamics of the light-matter interaction planar targets are usually used for convenience since in spherical geometry the high densities make optical measurements impractical (Fig. I-1).

When a target is exposed to a laser pulse,absorption of the laser energy creates a pressure distribution which can accelerate particles to velocities greater than the local sound speed, thereby creating a shock wave which compresses target material. However, at the laser intensities required to compress the target to the desired density hot electrons are produced which penetrate into the target and preheat the material. The net effect is that even a higher pressure

would be necessary to reach the required high density.

Therefore targets must be designed to minimize the production and transport of hot electrons. The pressure exerted on a target may be derived from the measurement of the transit time of shocks through the target. We will show that if the particle velocity behind the shock can be measured,it is possible to extract information about the density and therefore the equation of state or the relationship between the pressure and density. This equation is known approximately from theoretical calculations and therefore measurements which yield the density as a function of the pressure are of great importance for laser fusion studies.

In this thesis we propose to measure such high pressures and densities by the measurement of shock waves which are produced when an intense laser pulse irradiates a planar target. The theory of this method is described in Chapter II and is based on the understanding of (weak) shocks and expansion waves propagating through solid material. During the development of this theory we have noticed that the pressures and densities of the shock compressed matter can be found by the measurement of the propagation velocity of the shock and the unloading velocity of the shock compressed matter at the rear of the target. Moreover the diagnostic method has the advantage of extracting the pressures and densities without any knowledge of the microscopic physics. This investigation also shows

that the results are not significantly changed by the presence of any preheating

Following the theoretical development of this method we try to verify the diagnostic method using a two stage ruby laser. This laser was selected for its availability. in addition, there are not many recent measurements at the interaction wavelength of .69um which could complement the measurements of the often studied .503um and wavelengths. Chapter III describes the design of the laser and the diagnostic apparatus and Chapter IV gives the experimental results found with the streak camera and other diagnostic methods.

The picture of the laser plasma processes that can be drawn from this diagnostic method reveals a relatively weak perturbation even at our highest laser intensity, where shocks in the laser targets are only marginally established. For that reason, the proposed diagnostic method developed in Chapter II for strong shock waves is not yet employable. However we are able to verify the experimental results in another way by the use of an analytical heat wave model, that allows us to predict for instance the exhaust velocity when either the shock velocity or the laser intensity have been measured. This model is based on universal bremsstrahlung absorption and we find that the measurements and model agree quite well. This absorption mechanism is represented by a heating curve which gives the temperature of the exhaust plasma which one could put on the heating

another point on the Temperature vs. Intensity (heating characteristic) curve for laser plasmas. It is interesting that a universal heating curve exists for laser plasmas from which the exhaust temperature for the laser plasma can be predicted from the laser intensity alone.

The experimental results of Chapter IV are also in agreement with detailed numerical predictions of the Medusa hydrocode which we describe in Chapter VI.

All these results are summarized in Chapter VII, which also gives some suggestions for future work.

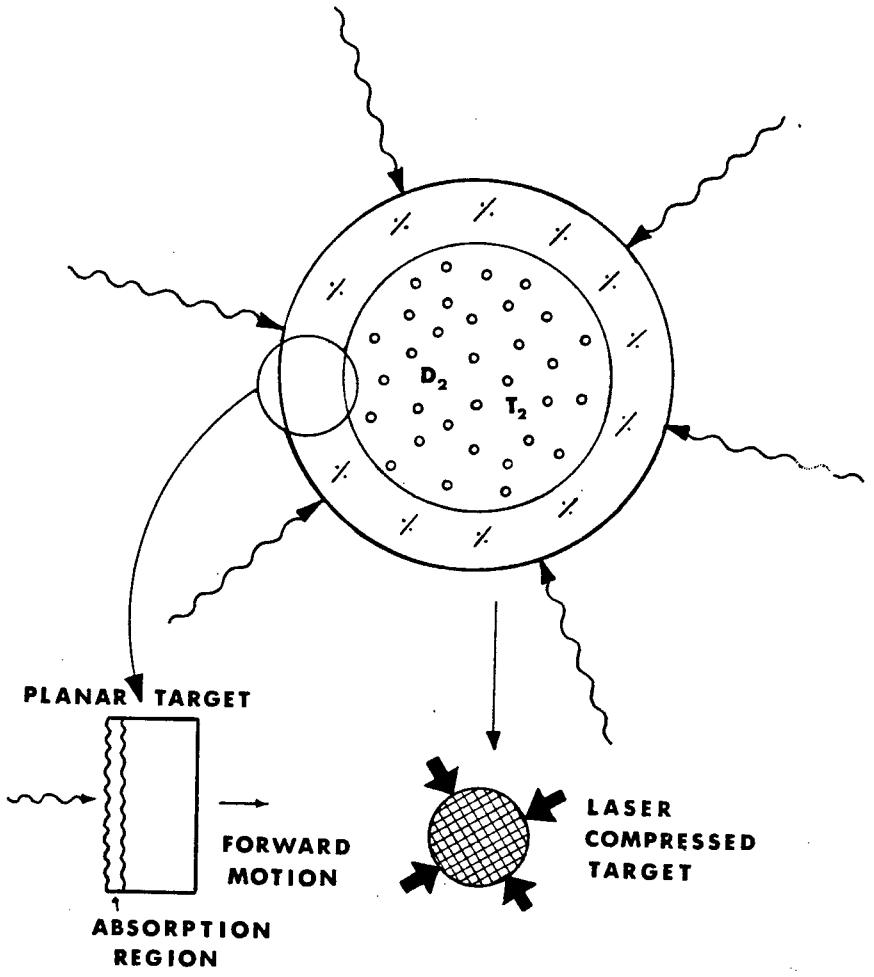

Figure I-1 Laser Target

Chapter II

Shock Wave Diagnostics on Laser Fusion Targets

Introduction

The deposition of an intense laser pulse onto a solid target causes violent motion in the forward and backward directions. This is known from many published streak photographs (Ref. 1-4). In this chapter we try to establish what information we can extract about this plasma from a detailed kinematic analysis of such streak photographs. Often one can see shock or expansion waves on the streak photos and one realizes that a thorough understanding of such hydrodynamic phenomena will be required in order to comprehend the motion fully. These shock waves occur if very high pressures are suddenly created in a medium and therefore it must be the laser pulse that is responsible for the creation of these high pressures.

Several methods have been proposed to measure the ablation pressure.

1) One way is to use as target a ballistic pendulum, and measure the total momentum(ref. 4).

$$MV = AP_a t$$

Where M=Mass, V=final velocity, A=Area of laser beam, t=duration of laser pulse. Difficulties arise if the

laser pulse is very intense, and the target continues to blow off plasma after the pulse has been turned off. Therefore this method tends to overestimate the ablation pressure created by the laser pulse.

2) Charge collectors have been used frequently to measure and count the debris which is released from the target. These charge collector signals are recorded as function of time, and by knowing the distance of the charge collectors from the target one can derive the velocity from the delay time of the ions released by the target. If there is only a single pulse,a blowoff velocity could be determined as function of direction. From such measurements the ablation pressure has been derived. Difficulties arise if there are more than one peak on the charge collector signal. Also this method lacks time and space resolution and it essentially measures only one quantity, namely the velocity of (unidentified) particles generated somewhere in the target blowoff plasma region.

3) A third method involved the direct observation of the shock front generated in the target material with time resolved photography. From the shock front velocity the ablation pressure is calculated using standard shock theory. Clearly the results will be wrong if there is any significant preheating, and furthermore one would need transparent targets for the optical observations.

4) Spectroscopic measurements of temperature and density in the blowoff region can be combined to obtain the

ablation pressure. These measurements appear to be the most accurate for the ablation pressure provided one can ascertain that n and T are indeed measured at the same place and at the same time. However these measurements do not reveal the parameters in the region ahead of the ablation front itself.

5) Finally the ablation pressure can be inferred from measurements of the burn velocity and one other parameter such as the exhaust temperature by using the conservation equations of mass momentum and energy across the ablation front.

In this thesis, we show another method of extracting the laser produced fluid parameters by the measurement of the unloading process at the rear of the target foils. This diagnostic method has the advantage of extracting the fluid parameters without any knowledge of the microscopic physics. Moreover the model shows how the energetic electrons which change the initial state of the target affect the results.

In order to understand the technique consider a foil (with a test gas mounted behind it) which as been struck by an intense laser beam (Fig. 2-3). As the intense laser pulse irradiates the target, the laser's energy is absorbed in a thin layer near the target's surface. The plasma which is produced on the surface of the solid target rapidly expands away from the target surface. To conserve momentum a shock is launched. This shock passes through the foil to the rear surface. At that instant the target material has an

increased pressure, density, temperature and a forward particle motion u_p. The physical situation is similar to that found in a conventional pressure driver shock tube, except that the pressure driver gas has the bulk particle velocity u_p.

It is well known that the kinematic motion of such a pressure distribution is entirely governed by the expansion wave relations and the fact that the pressure and particle velocity are constant across the contact surface, and by the jump conditions across the shock in the test gas. If the shock velocity in the foil and test gas are measured then we have the capability of measuring the equations of state of materials subjected to intense laser-generated shock waves.

As pointed out earlier in the introduction, problems arise if the laser light produces hot electrons. These electrons penetrate deeply into the target and the adjacent test gas, and can consequently change the material's initial state by preheating. If these electrons raise the initial temperature and pressure ahead of the shock front the Mach number decreases and consequently the shocked density and particle velocity all become functions of the Mach number (Fig. II-1).

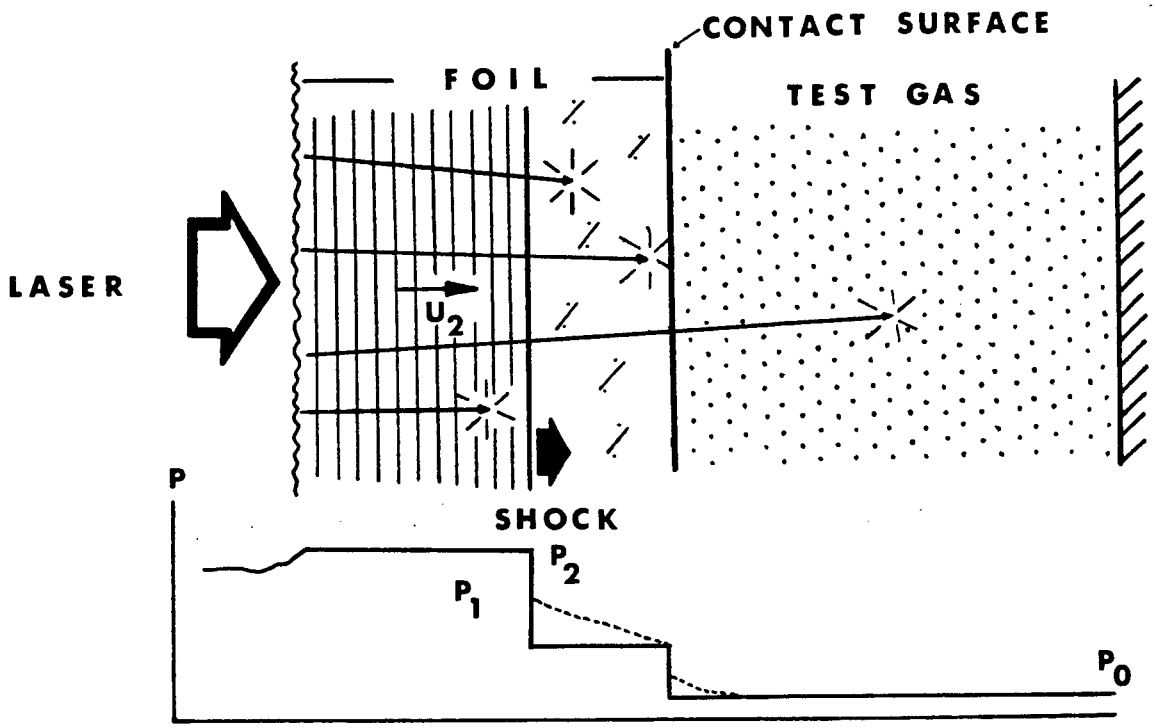

Figure II-1 Solid target exposed to laser light with test gas behind. Pressure distribution with and without preheat.

II-B Weak Shock Waves

The physical description given in the previous section can be described by the conservation equations for mass, momentum and energy. The subscript 1 refers to quantities ahead of the discontinuity and 2 behind the discontinuity.

$$\rho_1 v_1 = \rho_2 v_2 \tag{1}$$

$$p_1 + \rho_1 v_1^2 = p_2 + \rho_2 v_2^2 \tag{2}$$

$$\frac{1}{2} v_1^2 + h_1 = \frac{1}{2} v_2^2 + h_2 \tag{3}$$

where ρ is the density, p the pressure, and h is the enthalpy which is related to p and ρ by the equation of state.

$$h = \frac{g}{g-1} \frac{p}{\rho} \tag{4}$$

through the enthalpy coefficient g (ref. 18). The above jump equations can be solved in general form for the ratios of density and pressure (ref. 19).

$$\frac{\rho_1}{\rho_2} = \frac{v_2}{v_1} = \frac{v_1 - u_2}{v_1} = 1 + \frac{F}{g_1 M_1^2} \tag{5}$$

$$\frac{p_2}{p_1} = 1 - F \tag{6}$$

where

$$F = \frac{g_2 - g_1 M_1^2}{g_2 + 1} \left\{ 1 + \sqrt{1 - \frac{2(g_2+1)(g_1-g_2) M_1^2 g_1}{(g_2-1)(g_2-g_1 M_1^2)^2}} \right\}$$

and

$$M_1 = \frac{v_1^2}{a_1^2} = \frac{\rho_1 v_1^2}{g_1 p_1}$$

If the enthalpy coefficients g_1 and g_2 ahead of and behind the shock are equal, the second term under the root of F vanishes, and major simplifications result. Also if the Mach number M_1 is large, F vanishes.

In the absence of better knowledge the assumption is made that:

$$g_2 = g_1 \tag{7}$$

An estimate of the error introduced by this assumption is made at the end of the calculations. Compression ratio (5) and shock strength (6) can now be expressed for weak shocks as:

$$\frac{\rho_2}{\rho_1} = \frac{v_1}{v_1 - u_2} = \frac{g_2+1}{g_2-1+\frac{2}{M_1^2}} \tag{8}$$

$$\frac{p_2}{p_1} = \frac{2g_1 M_1^2}{g_2+1} - \frac{g_2-1}{g_2+1} \quad \ldots \text{ or } \quad p_2 = \frac{2\rho_1 v_1^2}{g_2+1} - p_1 \frac{g_2-1}{g_2+1} \tag{9}$$

and one can now give the sound velocity:

$$a_2^2 = g_2 \frac{p_2}{\rho_2} = \frac{2g_2\left(g_2-1+\frac{2}{M_1^2}\right)}{(g_2+1)^2} v_1^2 \tag{10}$$

and the particle velocity:

$$u_2 = \frac{2 v_1}{g_2+1}\left(1 - \frac{1}{M_1^2}\right) \tag{11}$$

The well known strong shock relations are found from (8) to (11) by letting M_1 approach very large numbers. Figure II-2 indicates how the particle velocity u_2 depends on the

enthalpy coefficient g_2 and the pressure ratio P_2/P_1 which is approximately equal to M_1^2 (see eq. 9).

II-C The Expansion Wave

Figure II-3 illustrates in a space-time diagram a shock propagating through a foil and test gas. The various regions are identified by index numbers. Figure II-4 shows the profiles of pressure and temperature and particle velocity at time t_3 when the shock has just reached the contact surface and at the time t_4 when the shock travels through the low density test gas. As shown in the Figure for velocity, there is an increase in the bulk velocity $u'=u_4-u_2$ of foil material after expansion by the rarefaction wave. It should also be pointed out that the particle velocity is constant across the contact surface ($u_3=u_4$).

The standard relation for a rarefaction wave is given by:

$$u_2 + \frac{2}{g_2-1} a_2 = u_4 + \frac{2}{g_3-1} a_3 \qquad (12)$$

where u_4, the particle velocity is directly related to the shock velocity in the test gas. The sound speed a_2 can be related to the initial shock velocity v_1 in the target foil by using relation (10). The standard relation $P\rho^{-\gamma}$=constant holds in the expansion process. If one knew the adiabatic exponent γ, a_3 could be related to P_4 since P_4 is an explicit function of v_4. However γ and the local

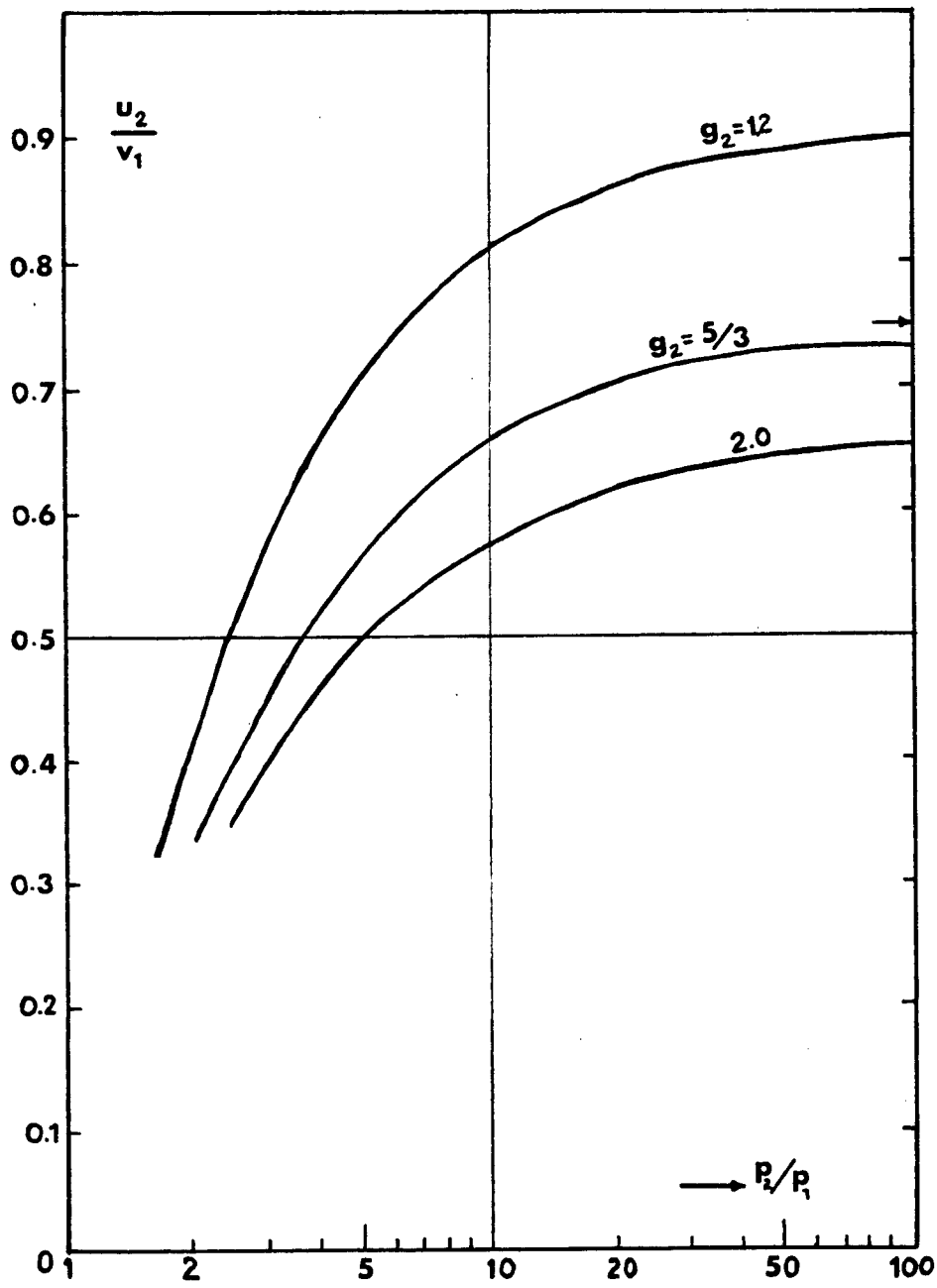

Figure II-2 Particle velocity u behind shock wave as a function of preheat pressure P .

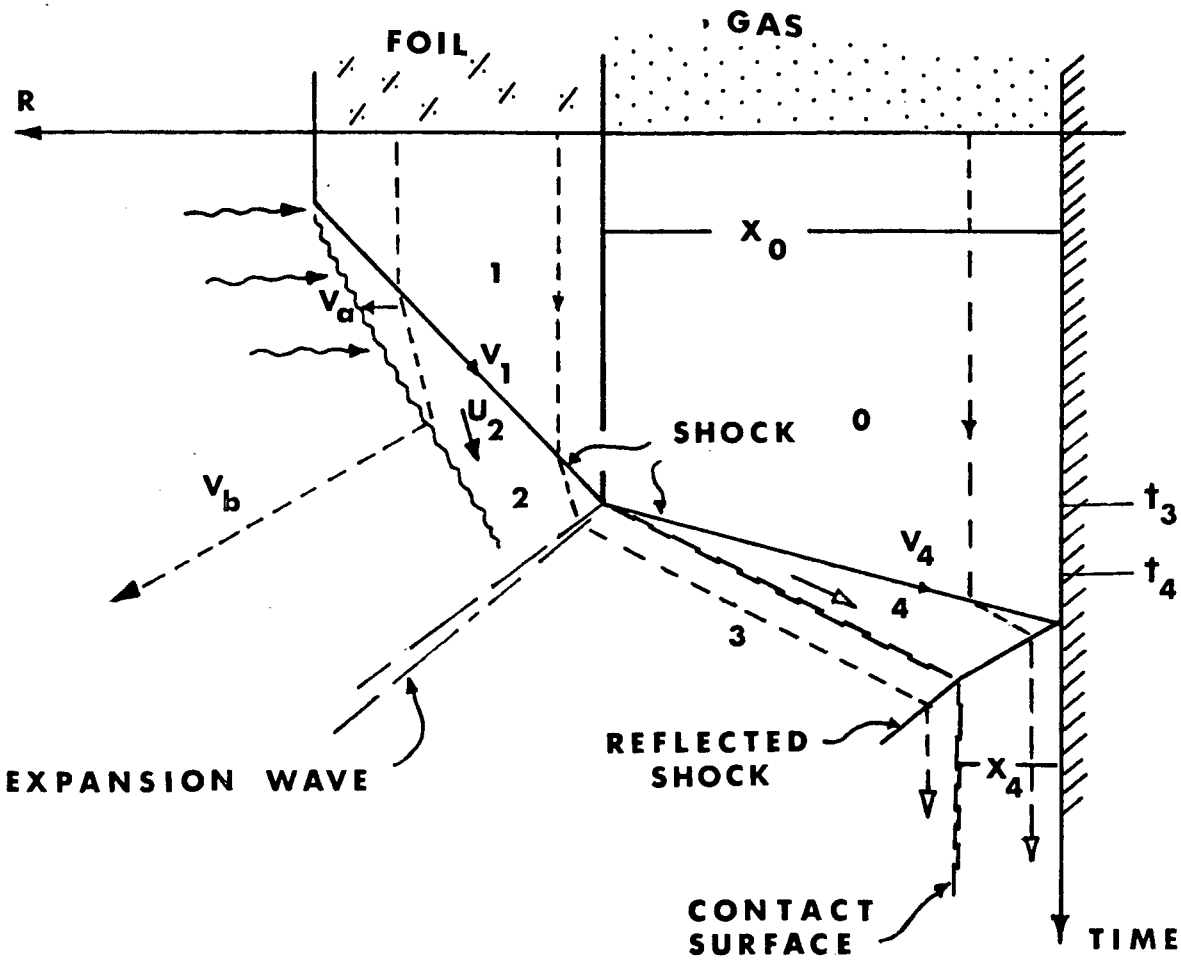

Figure II-3 Space time diagram for shock and expansion wave in foil and test gas.

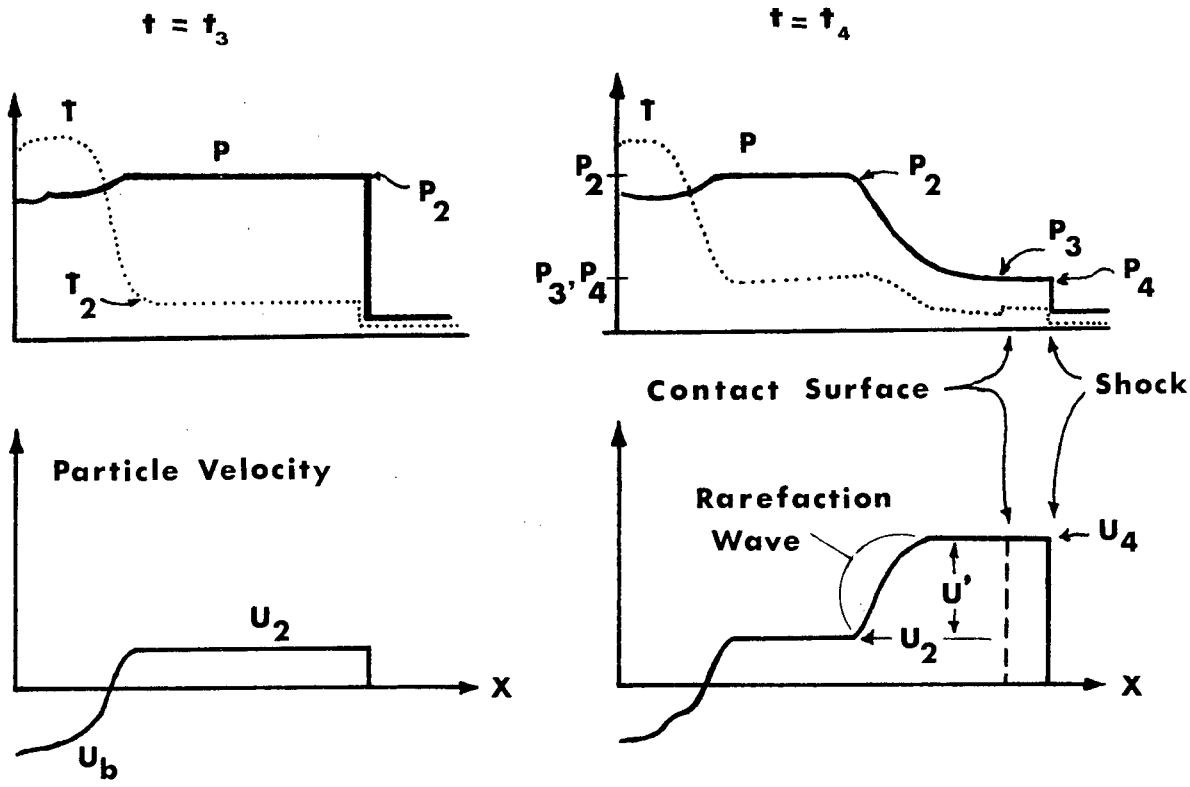

Figure II-4 Pressure, temperature, and velocity profiles at different times are identified in Fig. 3.

enthalpy coefficient g_3 are not known. Therefore, if a test gas with a very low density is mounted behind the target foil, u_4 would asymptotically approach the free expansion velocity u_{40} as the density ρ approaches zero. With these conditions the last term can be neglected and equation (12) becomes:

$$u_2 = u_{40} - \frac{2}{g_2-1} a_2 = u_{40} - \frac{2}{g_2^2-1}\sqrt{2g_2\left(g_2-1+\frac{2}{M_1^2}\right)} \quad (13)$$

Assuming that u_{40} and v_1 can be measured equation (13) can be used to determine the enthalpy coefficient g_2. For convenience u_2 is eliminated by the general shock relation (11) in order that the ratio of the measured values u_{40} and v_1 can be calculated as a function of g_2 and M_1. This is illustrated schematically in Figure II-5. It should be noted that the Mach number has only a minor influence on the results. If the ratio u_{40}/v_1 is known, even without the knowledge of the Mach number, the enthalpy coefficient g_2 can be determined with little uncertainty.

Also shown in Figure II-5 is the particle velocity u_2 as a function of u_{40}/v_1 and Mach number M_1. This has been derived by the use of equation (11) to eliminate g_2 from equation (13). Again even if the Mach number M_1 is not known and if u_{40}/v_1 is measured the particle velocity can be obtained with a tolerable uncertainty. For convenience the particle velocity u_2 is written in analytical terms and plotted as a function of $b(g_2, M_1, u_{40}/v_1)$ as defined by equation (13). Notice in Figure 6 that $b(g_2, M_1, u_{40}/v_1)$ is linear in u_{40}/v_1 and can be expressed as:

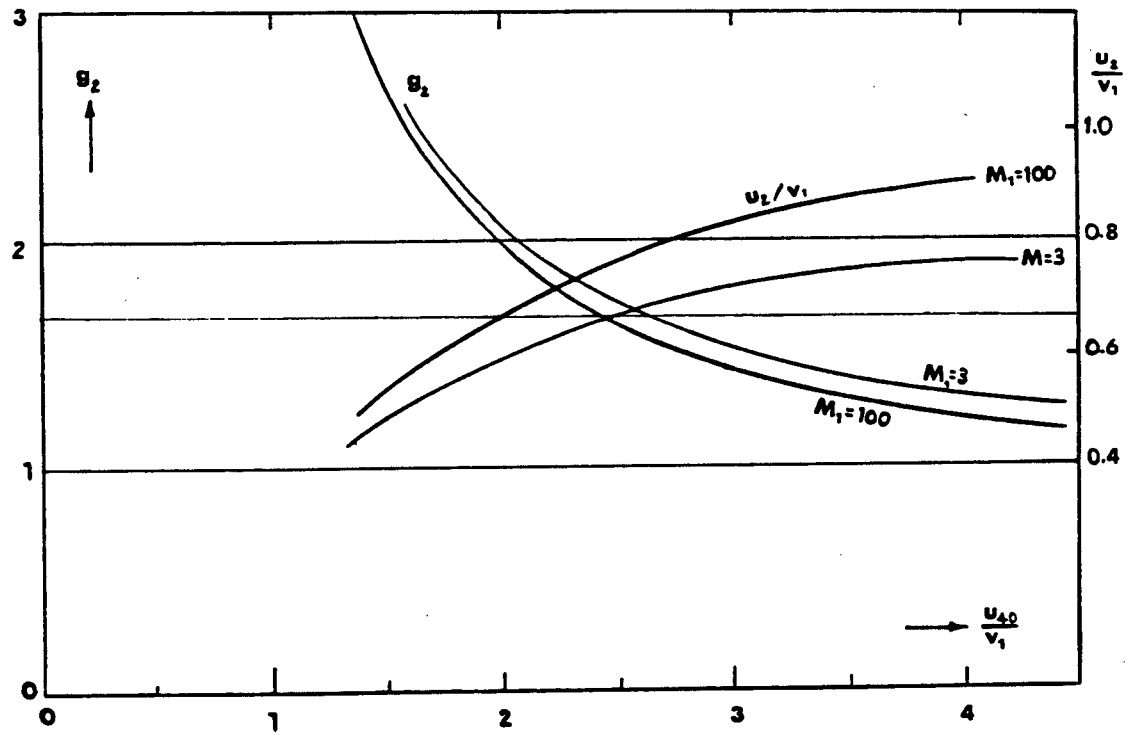

Figure II-5 Enthalpy coefficient g_2 and normalized particle velocity u_2 as function of the velocity ratio u_{40}/v_1.

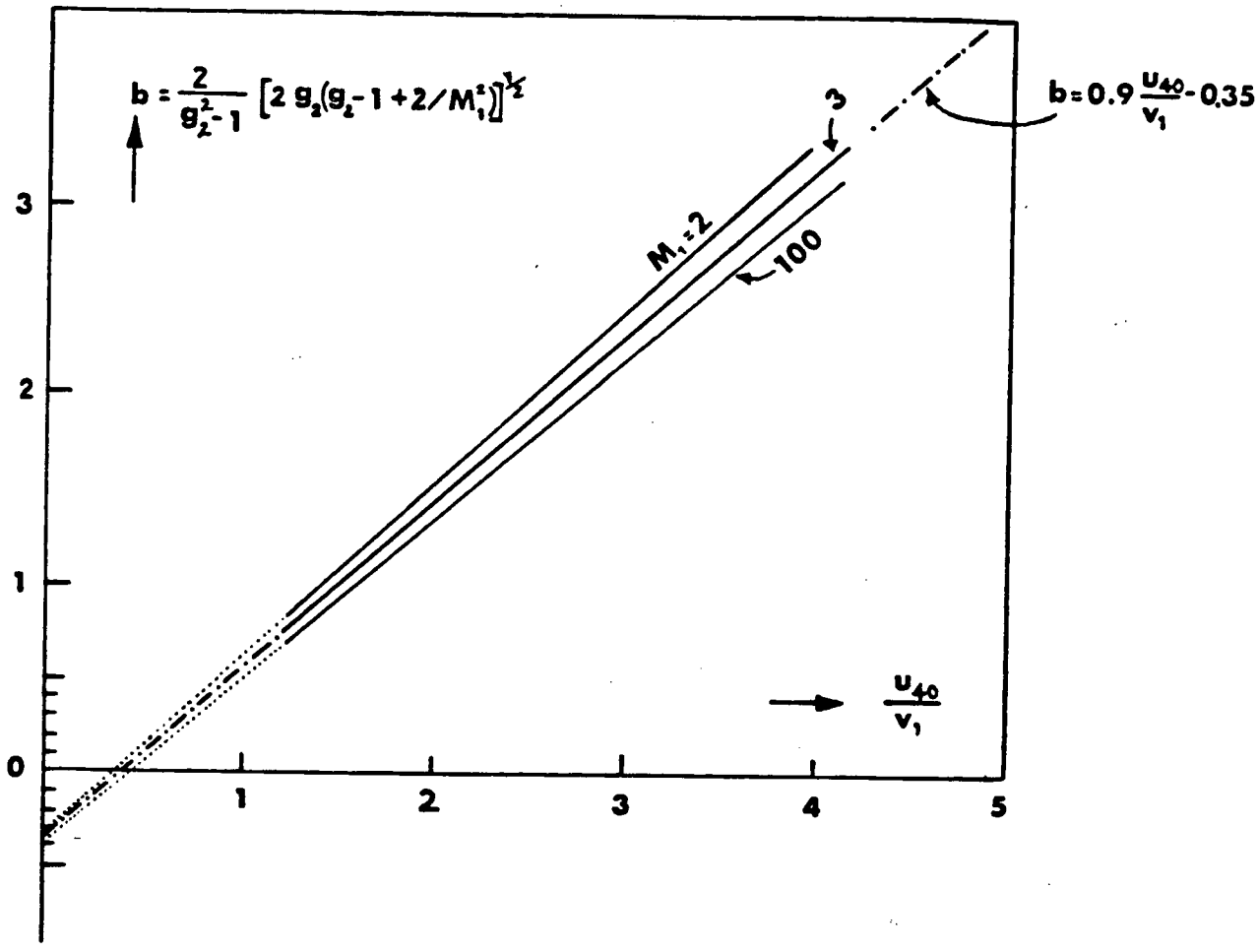

Figure II-6 Coefficient b as function of velocity ratio.

$$u_2 = 0.1\,u_{40} + 0.35\,v_1$$

$$b \simeq 0.9 \frac{u_{40}}{v_1} - 0.35 \qquad (14)$$

Hence by entering this result into equation (13) we have:

$$u_2 = 0.1\, u_{40} + 0.35\, v_1 \qquad (15)$$

Now the density within the shocked material can be written as:

$$\rho_2 = \frac{\rho_1}{1 - \frac{u_2}{v_1}} = \frac{\rho_1}{0.65 - 0.1 \frac{u_{40}}{v_1}} \qquad (16)$$

The pressure in the shocked foil may now be written as:

$$p_2 = \frac{2 \rho_1 v_1^2}{g_2 + 1} - p_1 \frac{g_2 - 1}{g_2 + 1}$$

where the preheat term may be neglected for Mach numbers exceeding 2. In principle, if the enthalpy coefficient g was known, the Mach number and therefore the preheat pressure P could be determined. However, from a careful inspection of Figure II-5, we find that the preheat pressure, P_1 is quite inaccurate since M_1^2 is not a sensitive parameter.

II-D The Shock in the Test Gas

At this stage we are already in the position to determine the fluid parameters if only v_1 and u_{40} are known; it remains to be shown how u_{40} itself can be found. For this reason we look at the details of the propagation of the shock in the test gas. At higher test gas densities a well developed shock wave is formed where the particle velocity is related to the shock velocity v_4 by the standard

relation:

$$u_4 = \left(1 - \frac{\rho_0}{\rho_4}\right) v_4$$

It may be possible to extract the compression ratio ρ_4/ρ_0 from streak photos, if the contact surface at the reflected shock is resolvable. In this case from Figure II-3 we have

$$\frac{\rho_4}{\rho_0} = \frac{x_0}{x_4}$$

so that u_4 can be written as:

$$u_4 = v_4\left(1 - \frac{x_4}{x_0}\right)$$

This relation is valid irrespective of any preheating of the test gas. On the other hand if such a measurement is not possible one can still estimate that the shock should have a Mach number of at least $M_4=4$. If the test gas density is low, the strong shock approximation is reasonably accurate for the particle velocity in the test gas. The strong shock relation is given by:

$$u_4 = \frac{2\ v_4}{g_4+1}\left(1 - \frac{1}{M_4^2}\right) \approx \frac{2\ v_4}{g_2+1}$$

Moreover the condition $M_4=4$ is found by assuming the test gas is preheated to the temperature T_2 obtained behind shock in the foil.

This concludes the kinematic analysis of the hydrodynamic flow. In the next few chapters subsequent experiments are presented which show the applicability of our model.

CHAPTER III

Experimental Apparatus and Procedure

A) Introduction

A system consisting of a 100MW ruby laser, a target chamber, a target holder, and an optical setup has been used to attempt to experimentally verify the model outlined in the last chapter. Figure III-2 shows the overall experimental layout and Figure III-5 shows the optical setup.

B) The Ruby Laser

The ruby laser serves both as a source of high intensity monochromatic light (40nsec halfwidth, 100MW power) and for the side on backlighting illumination of foil targets.

The laser system is similar to that used by Albach (ref. 7) and Godfrey (ref. 8). For details on the construction of the system refer to Churchland (ref. 9). A brief operational description of the optically pumped ruby system, also described by Hilko (ref. 10), is given in the next paragraph.

Four Xenon gas flashlamps surround a ruby rod all enclosed in a polished multi-elliptical reflector. The flashlamps are used to create a population inversion in the

chromium impurity ions of the ruby crystal. A 40ns, 100 MW laser pulse is produced by Q-switching.

The Q-switch or optical shutter is a Pockels cell in combination with a calcite polarizer. The ruby rod is pumped with flashlamps and a population inversion builds up. The Pockels cell is a birifrengent KDP crystal. When the crystal has 8800V applied between two faces, birifrengence is induced in the crystal. When radiation passes through the crystal it becomes circularly polarized. Upon reflection from the back mirror the radiation again passes through the KDP crystal and becomes plane polarized 90° to the original polarization. This radiation is then rejected by the polarizer. When the population inversion within the crystal is a maximum the Pockels cell is switched off and the plane of polarization of the radiation is unaffected. This allows a buildup of laser light within the cavity via feedback within the ruby crystal. Since the rear mirror is 50% reflecting the light leaves the cavity and is amplified.

C) The Pindiode and Gentec

To characterize the temporal shape and monitor the relative laser power output from shot to shot a Hewlett Packard 5082-4200 pindiode detects the laser light which reflects from the target chamber window. An oscilloscope trace records the light signs. A typical pulse is shown in Figure III-1.

This signal shows that the laser system produces a 40ns

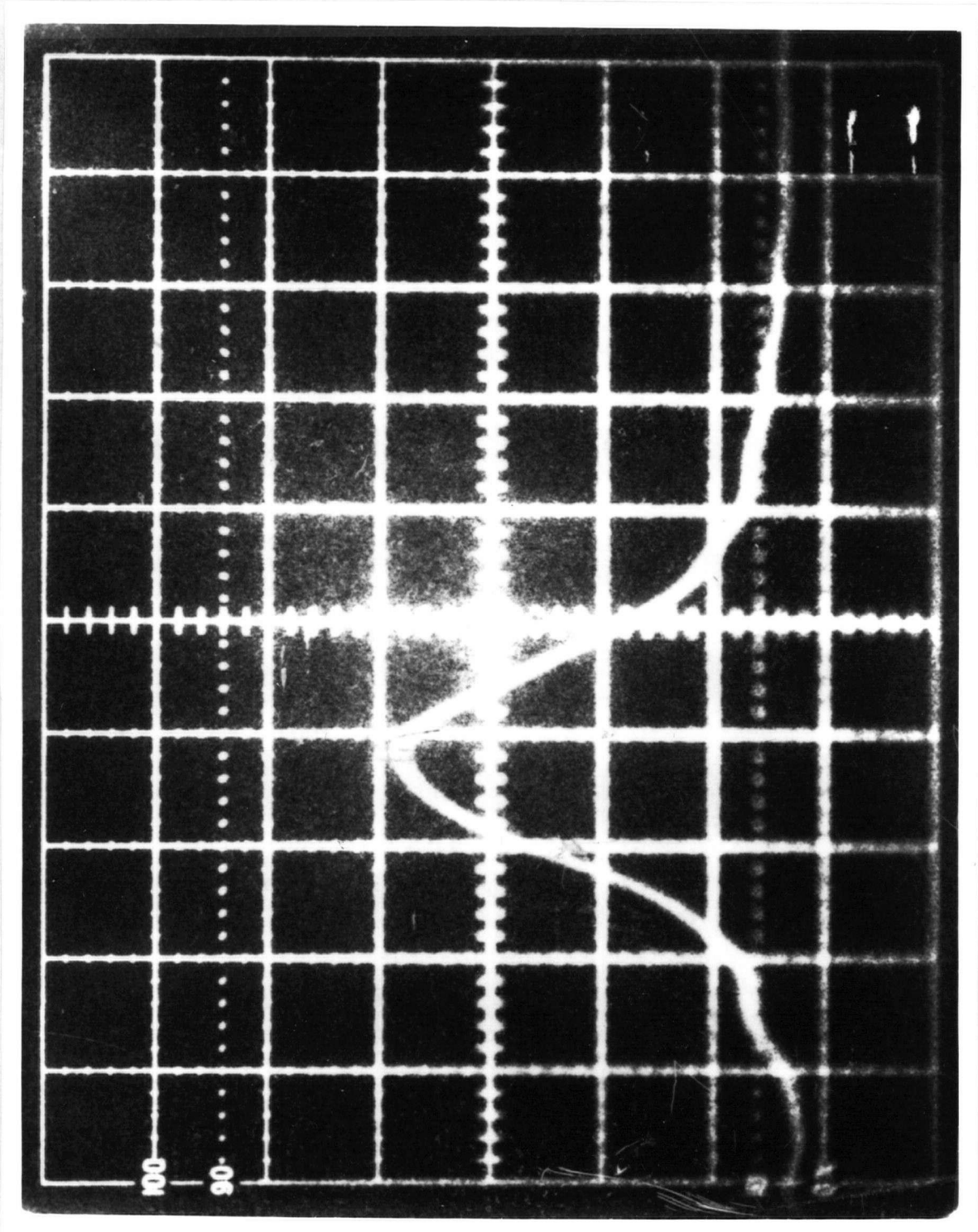

Figure III-1 Oscilloscope trace of the laser pulse Horizontal deflection 20nsec/div. vertical deflection 28 MW/div.

full width half maximum (FWHM) laser pulse.

The output energy of the system was detected with an energy meter. The laser system is capable of producing 15J of energy. However it was discovered that to maintain the optical components without damage, the system was operated to a maximum level of only 4.0J. The laser system had excellent reliability if the ruby rods were allowed to cool from shot to shot. Typically the time taken between shots was fifteen minutes.

D) The Target Chamber and Target Holder

The target chamber, as shown in Figure III-2, was constructed to ensure that breakdown would not occur in the gas which surrounds the solid target. At the power intensities used in these experiments, a high pressure gas would be very strongly ionized and the resultant plasma would absorb the laser light before it reached the target. The vacuum chamber was evacuated to 300 millitorr to maintain a uniform background pressure. This pressure maintains the same initial conditions for the expansion of the foil target.

Inside the target chamber is a target holder. The target holder must satisfy several conditions (Figure III-2) and the difficulty in designing an appropriate holder is firstly that one wants to load a set of targets for several shots since replacing a target between shots is time consuming, and secondly the targets must remain in the same

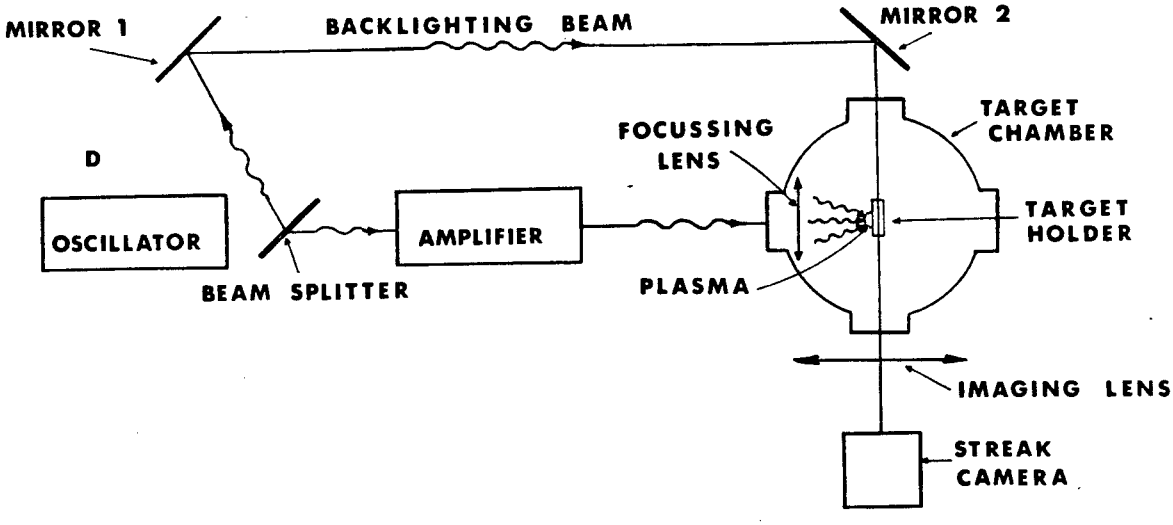

Figure III-2 Overall Experimental Layout

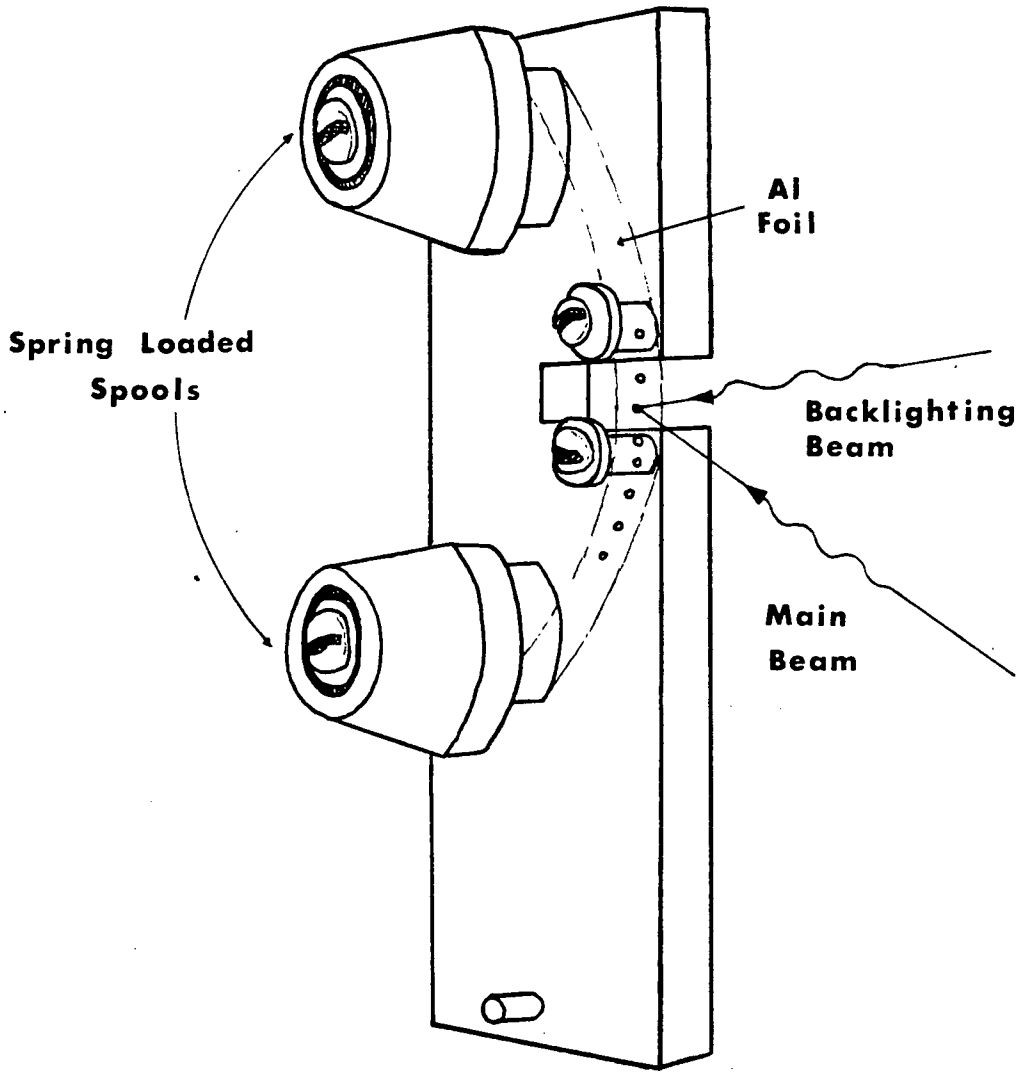

Figure III-3 Target Holder

focal plane to ensure the same flux on target. Thirdly the holder had to be designed to allow the imaging of the back surface and the side of the foil simultaneously. Fourthly, two of these target holders used together will allow for double foil experiments. As shown schematically the final design satisfies all the above criteria. Foil targets 50cm long, 50cm wide and 37.5 microns thick were wound on spring loaded spools (Figure III-3). Figure III-3 shows how the long strips of foil allow for multiple shots. By turning the spools the foil winds from one spool to the other, placing an unpunctured part of the foil in the aim of the main beam. The spools are spring loaded to keep a constant tension on the foil strip so that it remains in the same focal plane.

E) The Streak Camera

A TRW streak camera (ref. 11) which makes space-time plots has been used to observe the plasma. The general operation is best illustrated with the aid of Figure III-4.

When light is imaged by the objective lens onto the photocathode of the image converter tube electrons are emitted from a photosensitive material within the tube. The number of electrons emitted from a point on the material is proportional to the number of photons at that position. These electrons are accelerated by a radial electric field (15kv) applied between the anode and the cathode. These electrons are swept vertically by a ramp voltage applied to deflection plates. The rate at which the electrons are swept

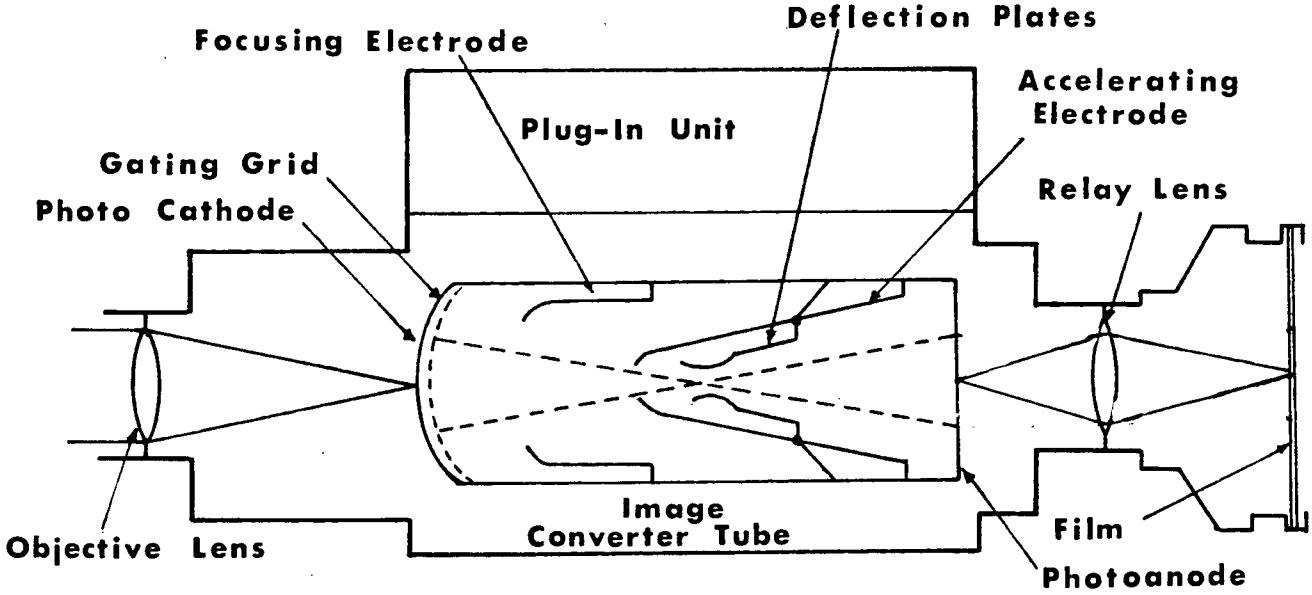

Figure III-4 Schematic diagram of Model 1D Image Converter Camera Head

is directly proportional to the slope of the ramp. When the electrons strike the photocathode, an intensified image is created on the anode and this image is relayed by the lens on the right into the film plane and thereby a space-time image is traced. A 10Kv voltage is applied to the grating grid to allow electrons to flow only when the grid is properly pulsed. The exposure time was set at 200ns duration.

The streak times used in this study were set at 200ns and 100ns. Streaks shorter than 100ns were impractical since the ramp voltages were not synchronized in time. This is a consequence of the impedance mismatch of the deflection plate circuitry. Several attempts were made to match the impedance of the ramps but synchronization was limited to approximately 50ns.

The spatial resolution of the photoanode which is 10 lines/mm or 100 microns fixed the temporal resolution (i.e., slit width). Since there is a 4:1 reduction of the object size at the film plane, the slit width was set at 400um for maximum spatial resolution (i.e., 100um). To first order the temporal resolution is the time it takes the slit to move its own width. The streak length is 5cm and therefore the writing rate is:

$$v = \frac{d}{t} = \frac{5 \text{ cm}}{20 \text{ ns}} = 2.5 \times 10^7 \text{ cm/sec}$$

Therefore the temporal resolution is given by:

$$t = \frac{d}{v} = \frac{100 \text{ cm}}{2.5 \times 10^7 \text{ cm/sec}} = .4 \text{ nsec}$$

One very bad feature of the available camera is the property that the width of the image depends on the intensity of the light. If the intensity changes the width of the intensity changes too. When the intensity of the backlighting beam was adjusted to ensure uniform streaks, streak duration was only 5ns, making a velocity measurement impossible. Therefore the intensity of the backlighting beam had to be carefully adjusted in intensity to ensure as uniform a streak as possible. This pinching could be an ion focusing effect due to gas leakage in the tube (i.e., an old tube).

F) Jitter and Timing of the Laser Streak Camera

All Q-switched lasers have jitter. To measure the ruby laser jitter several streaks were made of the laser pulse with the camera. Since the jitter of the laser system is a random process the root-mean square of the arrival time of the laser pulse has been taken. The laser jitter was found to be 40ns which corresponds to the FWHM of the laser pulse. It should be pointed out that this can be considered jitter in the camera and not the laser system since the experimental event is synchronized in time (i.e., with respect to the backlighting beam and the main pulse). Since streak durations are 200ns in duration each shot in theory should record an event. (Refer to Fig. III-7).

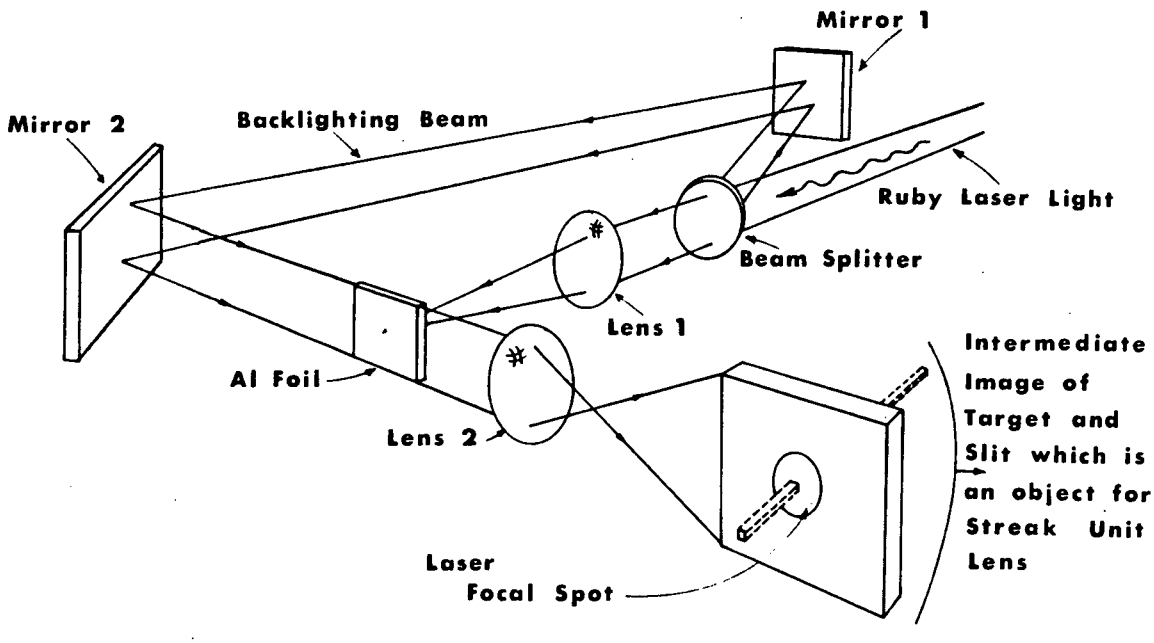

Figure III-5 Optical setup for laser-parameter foil experiments

H) Experimental Procedure and Optical Setup

In order to check the validity of the model presented in Chapter II, the TRW streak camera (ref. 12) has been utilized to record different laser plasma events. Figure III-3 shows the parameters which may possibly be measured. The two parameters which must be measured to validate the model are u_{40} and v_1. However all parameters are of interest and Figure II-3 shows all these parameters.

Figure III-5 shows the optical setup. The lens L_1 with f number of 2.5 and focal length of 10cm focusses the beam onto the target. A beam splitter has been inserted into the beam path behind the oscillator cavity at 45° to the main beam. This split off beam, called the backlighting beam, is spatially filtered (not shown in Figure III-5) by a pinhole and then by reflection from two mirrors passes the target 90° to the main beam. A f/2.5 lens forms an intermediate image onto the camera slit. This 20X magnified image is then imaged by the streak camera optics (Figure III-4). This setup allows for 4 different types of streak photos to be taken. The first type of streak photo is obtained by blocking off the main beam. This produces a streak of the backlighting pulse of a stationary foil (Figure IV-5).

For the second type of streak photo both the main and backlighting pulse are present so that a shadowgram of a laser produced plasma is produced (Figure IV-6). These shadowgrams depend on the bending of the ruby light and record the time history of the event when the main beam is

focussed and fired on target. A 6943 Angstrom filter was placed in front of the streak camera's objective lens to allow only the ruby light to enter the camera.

For the third type of streak photographs, the beamsplitter, the backlighting beam and the ruby filter were removed. So that one obtains records of the plasma expansion, example Fig. IV-5. There is however a chance that some of the scattered light from the main beam can reach the camera. To differentiate between this scattered laser light and the plasma light a fourth mode of operation was used. In this case the backlighting beam was turned off and the 6943 Angstrom interference filter was inserted, so that only the scattered ruby light could be recorded. This allows a comparison of streak photos with and without the filter so that the plasma light can be discriminated against the ruby light.

In order to measure the ablation velocity v_a a solid piece of aluminum was irradiated. By knowing the burn depth and the pulse length an upper limit to the ablation velocity can be calculated. However, we found that the velocity v_a is invalid since the target material is ionized and it continues to emit plasma material after the laser pulse is off.

To monitor the amount of incident laser energy which reflects from the target surface a beam splitter was placed in front of the focussing optics. Figure IV-1 shows how the backreflected light has been monitored with a gentec-oscilloscope combination.

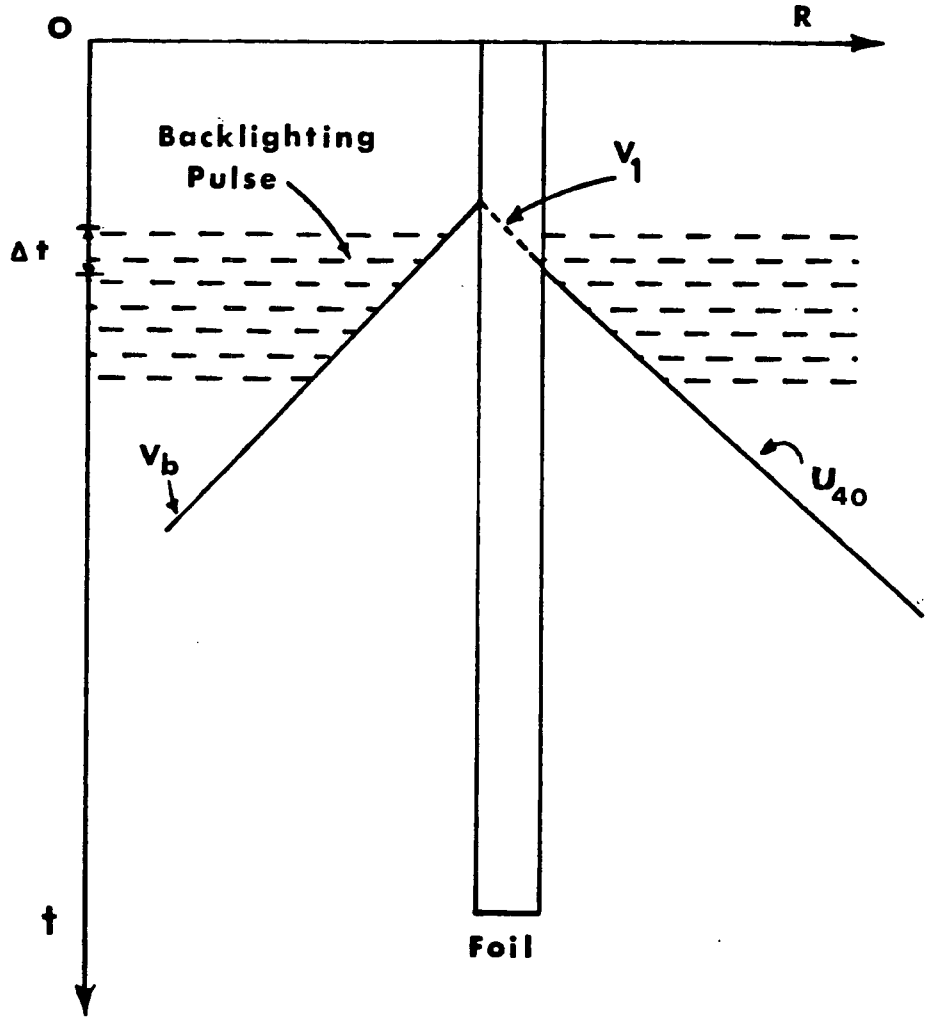

Figure III-6 Ideal space-time travel

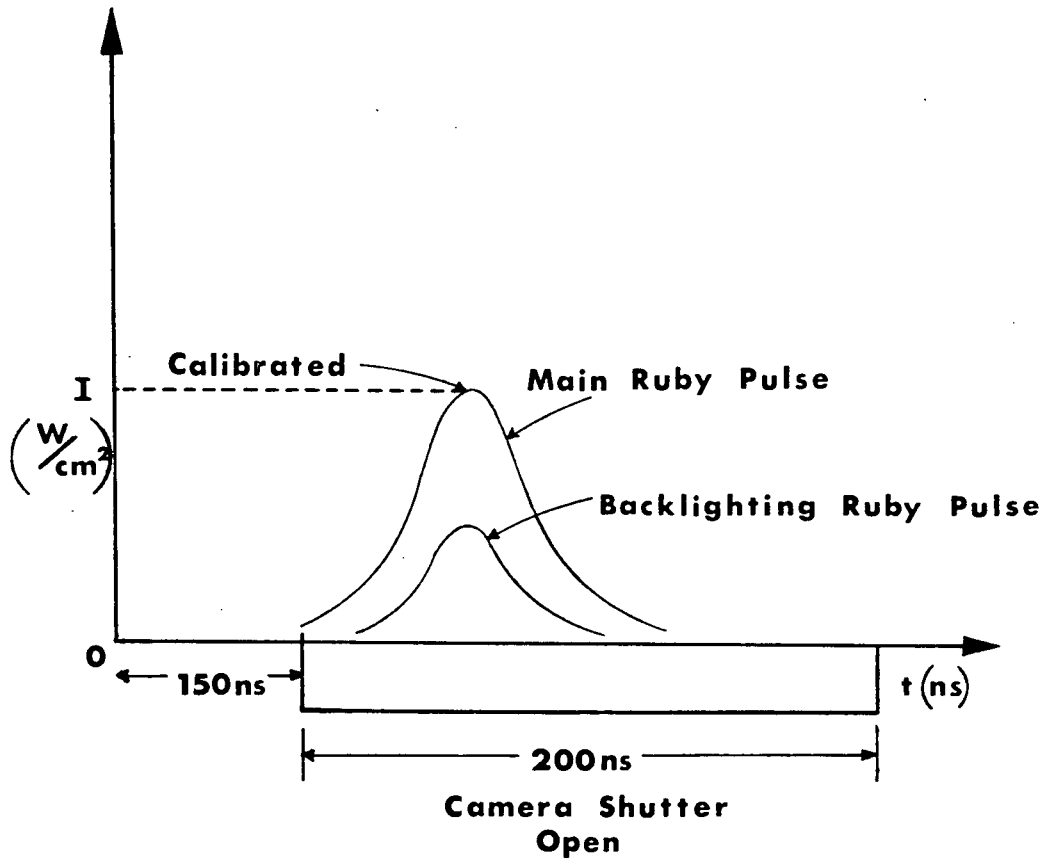

Figure III-7 Timing Sequence

Figure III-6 shows an ideal side-on streak photo of an expanded plasma with a backlighting pulse (horizontal dotted lines). The solid line labelled v_b indicates the leading edge of the exhaust plasma. By measuring the slope one can find the exhaust velocity, v_b . The shock wave passing through the foil cannot be observed directly but one can see plasma emerging on the rear of the target after the breakthrough at time Δt , so that the approximate path of the shock may be sketched (broken line) and the velocity v_1 obtained from the slope. The slope u_{40} of the plasma front on the rear of the target gives the unloading velocity of the accelerated foil material.

Figure III-7 shows the timing sequence for the arrival time of the main pulse and backlighting pulse with respect to the opening of the camera shutter.

CHAPTER IV

The Laser Power Determination and Experimental Observations

This chapter presents the laser power determination and the experimental results obtained with the methods which were outlined in the last chapter. As stated in the introduction the main motivation for this study has been to extract all the laser produced fluid parameters without any knowledge of the microscopic physics from the measurement of the shock transit time through the foil and by the measurement of the velocity of the shock compressed material unloading into a test gas.

It should be pointed out that the inherent difficulty in these experiments are the extremely small distance and time scales. The focal spot size is 100 microns while the physical events are occurring on time scales of 10^{-9} seconds.

The quantities which have been measured are the net absorbed power W, the exhaust velocity and the particle velocity of the accelerated foil material.

A) Net Power Flux

The output beam of the ruby laser system was focussed with a 10cm focal length lens onto the surface of solid aluminum targets. The net absorbed intensity is calculated by the measurement of the absorbed energy, the FWHM pulse

width, beam divergence and the focal length of the lens.

The focal length of the lens was measured by shining a He-Ne laser beam through a plano-convex lens a distance x from the centre. The deviation d of the light rays was then measured a distance s from the lens. Figure IV-2 shows the experimental arrangement and from the geometry the focal length f is given by:

$$f = \frac{xs}{d}$$

Several measurements were taken and the root mean square calculated. The focal length f equals 10 cm ± .1cm. This result agrees with the manufacturer's specification.

The beam divergence is found by taking a near and far field burn pattern. By knowing the distance between the two burn patterns and the increase in area of the burn pattern the beam divergence was found to be a milliradian.

Figure IV-2 shows focal spot size as a function of the focal length f and the beam divergence α . From the geometry, the focal spot size is calculated to be:

$$fs = f\alpha = (10\ cm)(10^{-3}) = 100\ um$$

As presented in Chapter III the ruby laser output energy is 4.0J, however, not all of the incident energy on target is absorbed. Figure IV-1 shows how the backreflected light has been monitored. These measurements show that of the 4.0J incident on target 50% of the energy is absorbed, while the other 50% is reflected and transmitted.

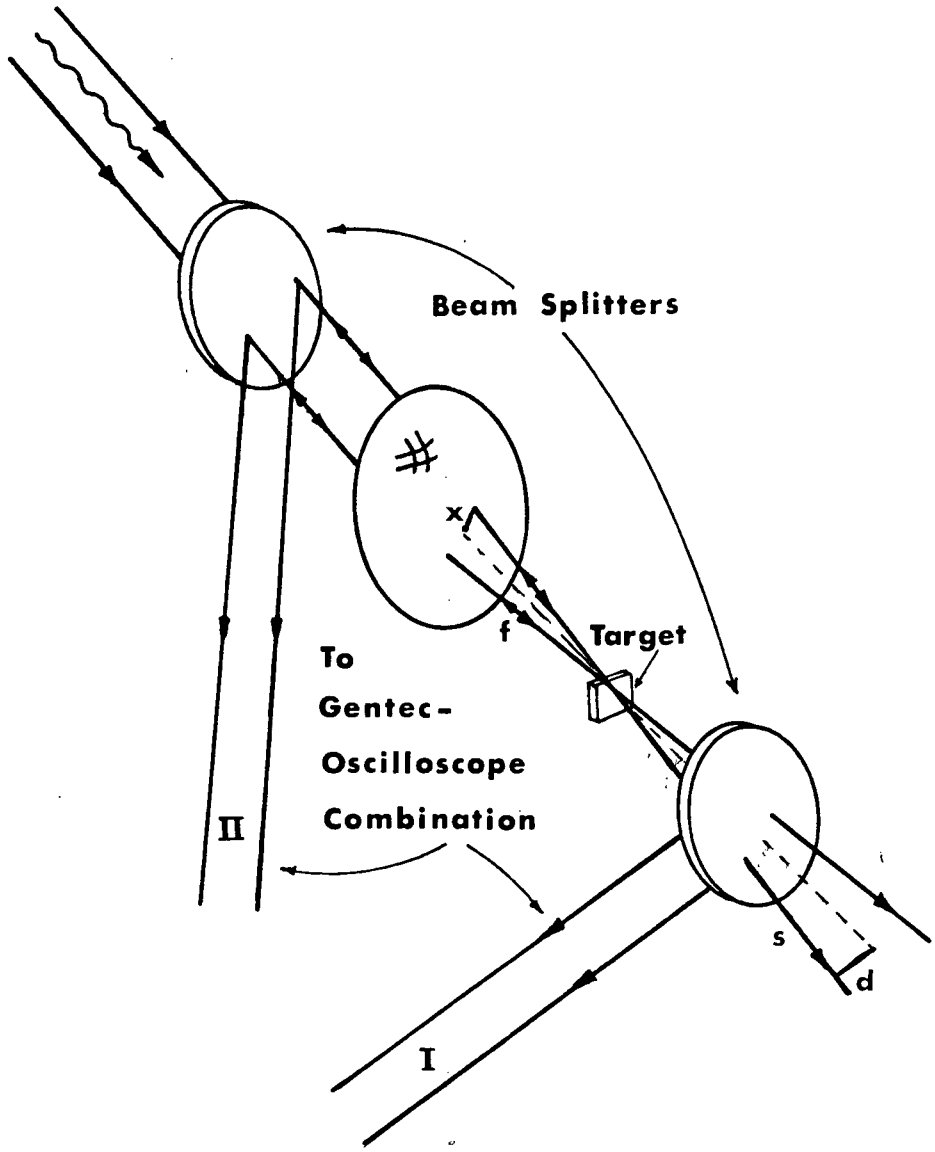

Figure IV-1 Setup for focal length determination and backreflection diagnostic. Beam I is used to determine the transmitted intensity and Beam II is used to determine the reflected intensity.

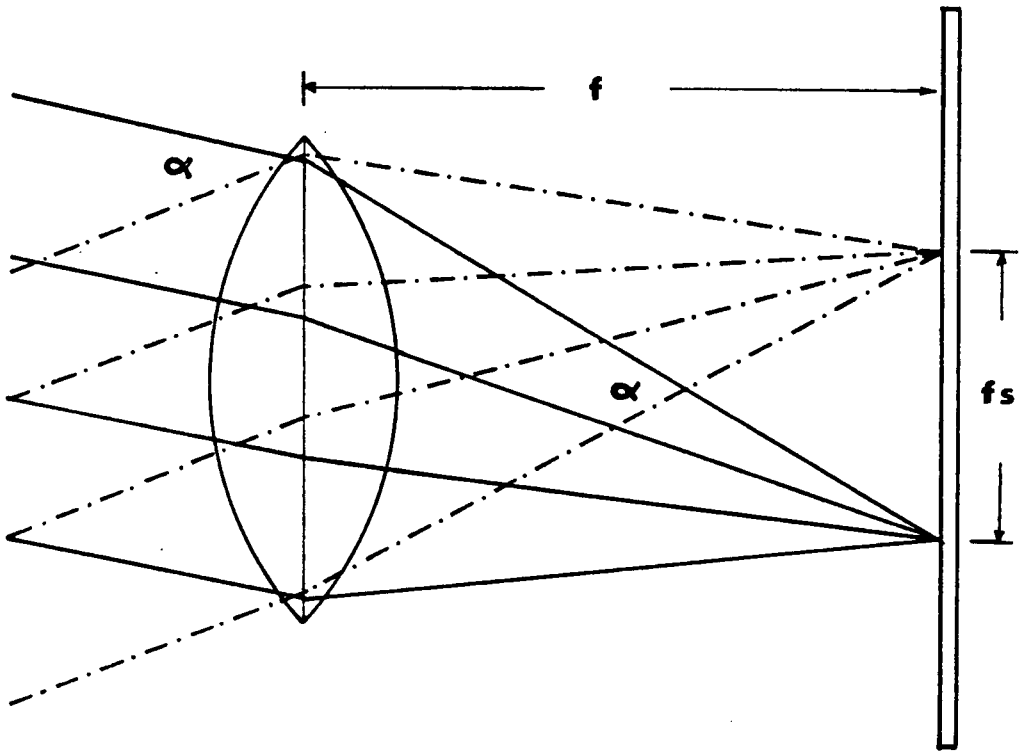

Figure IV-2 Ray-trace to determine the focal spot size

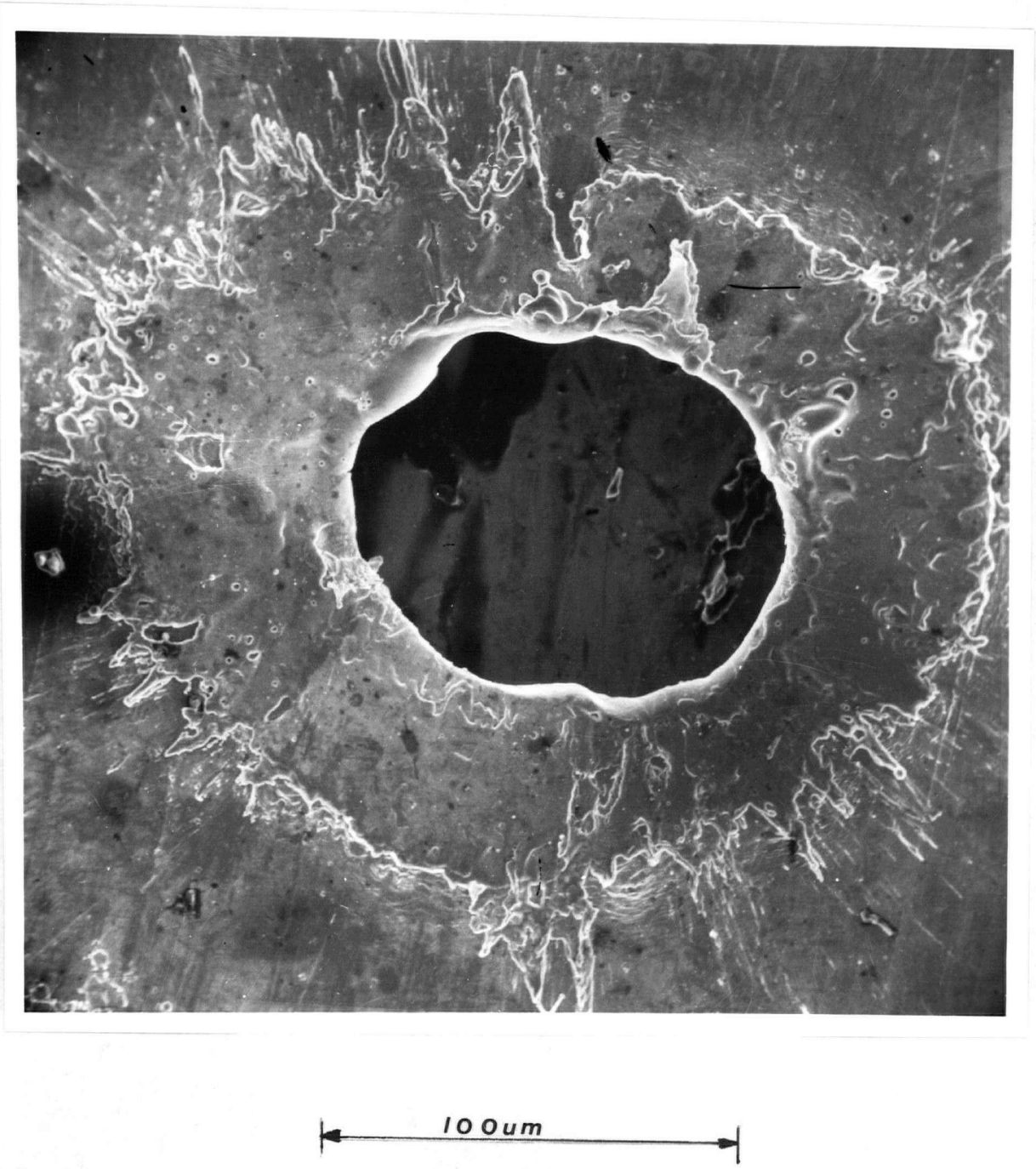

Figure IV-3 The hole punched through foil by laser

Therefore the net intensity on the target is:

$$W = \frac{\eta E}{t\pi r^2} = \frac{(.50)(4.0 \pm 10\%)}{(40 \times 10^{-9})(\pi \frac{112}{2} \times 10^{-4} \pm 10\%)^2}$$

$$W = 5.0 \times 10^{11} \frac{W}{cm^2} \pm 30\%$$

where r is the focal spot radius.

Figure IV-3 shows an electron micrograph of a hole in aluminum produced by the ruby system. Notice the agreement of the focal spot size with the above calculation.

B) Exhaust Velocity

A second quantity which was measured and is of interest is the expansion velocity of the foil material. This velocity can be attained from the streak photos recorded with the TRW streak unit. Figure IV-4 shows a typical streak of a stationary foil before the removal of the backlighting beam, pellicle beam splitter, and the 6943 Angstrom interference filter.

The average expansion velocity calculated by taking the slope of several streak photographs is 9 x 10^6cm/sec.± 10%. Figure IV-4 shows a typical streak from the photos which were analyzed. These streak photos are reproduceable from shot to shot.

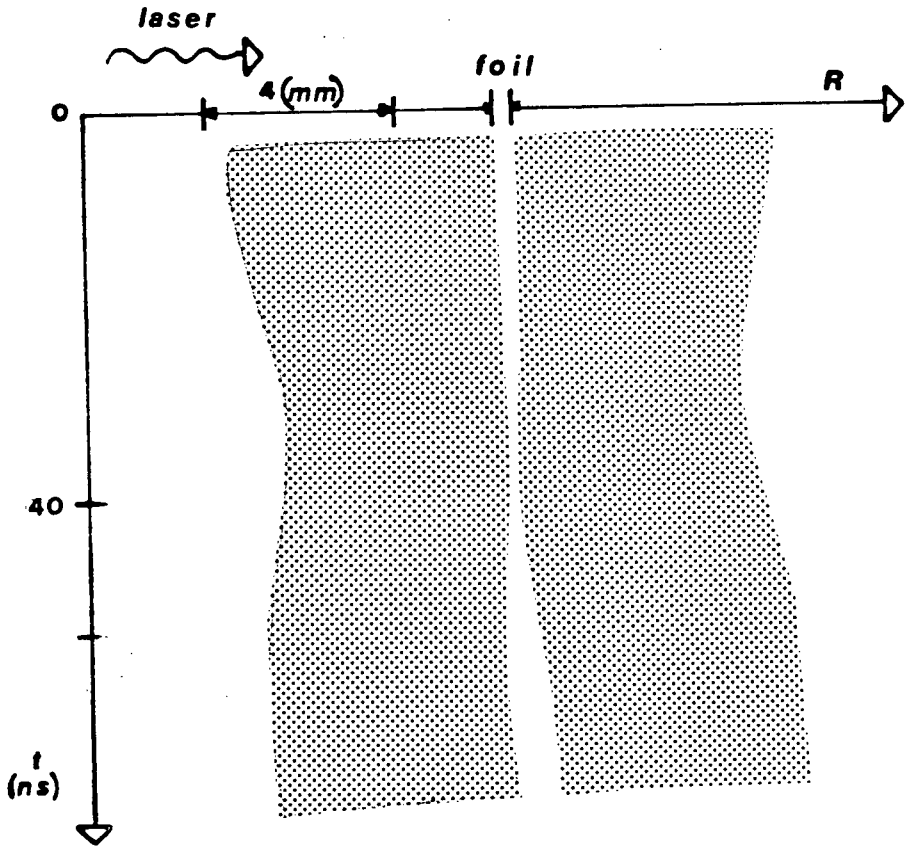

-dotted area shows the streak of the backlighting pulse

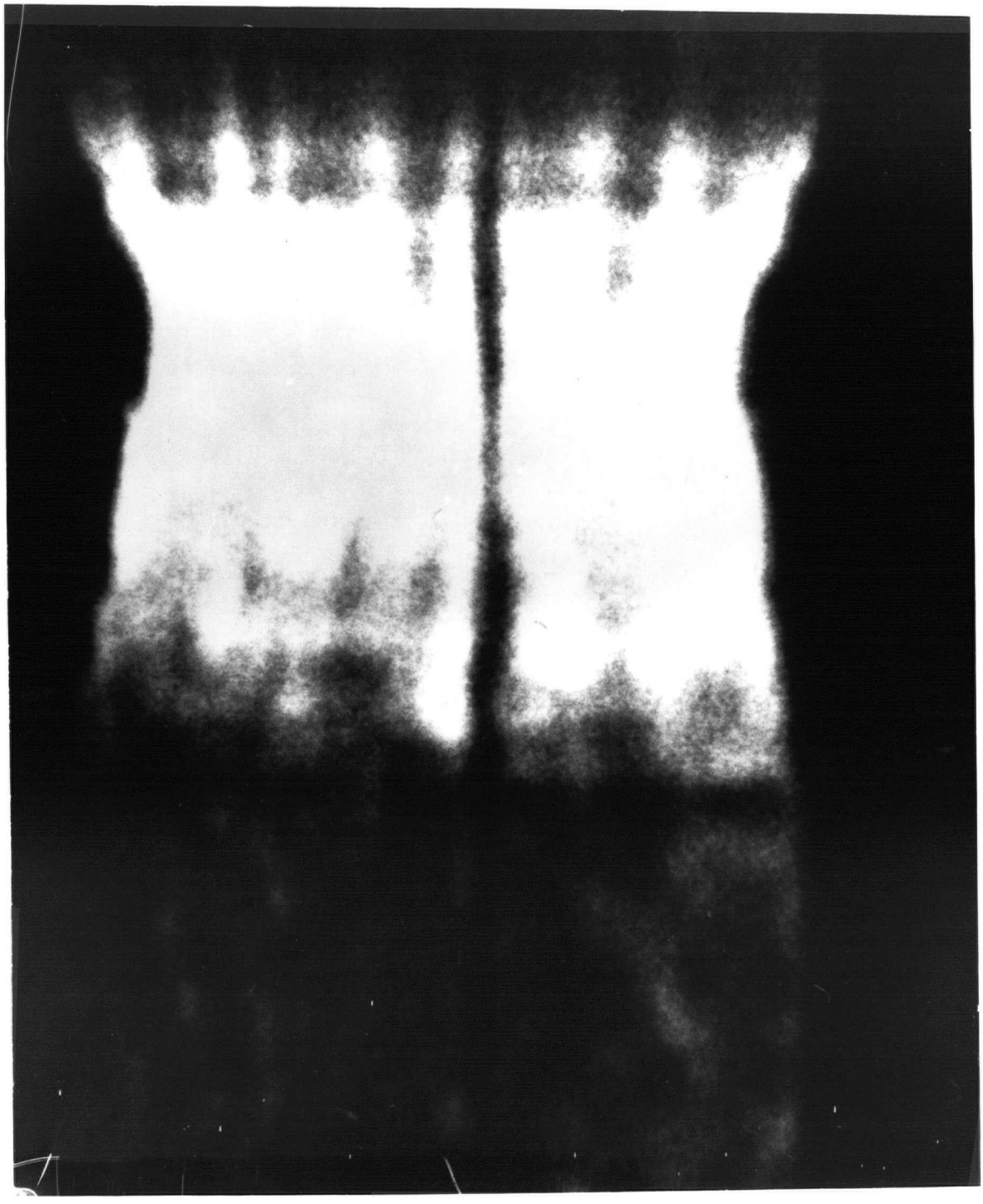

Figure IV-4 Streak photograph of laser pulse backlighting a stationary foil

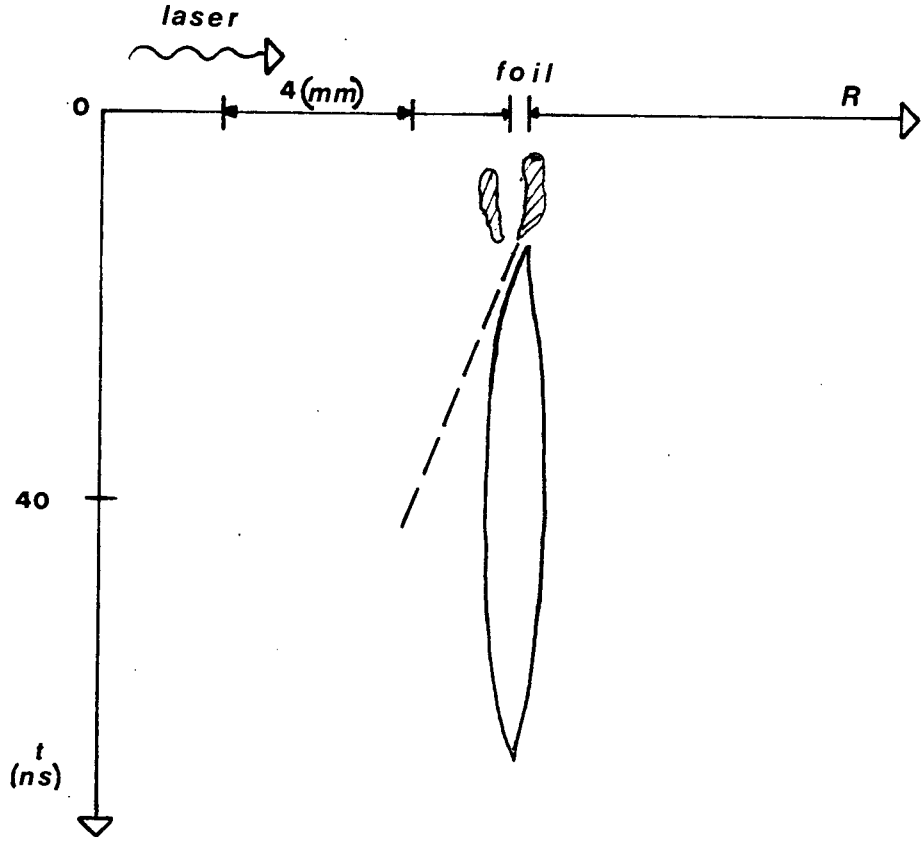

-hatched area shows scattered ruby light

-slope of the dotted line indicates leading edge of the exhaust velocity

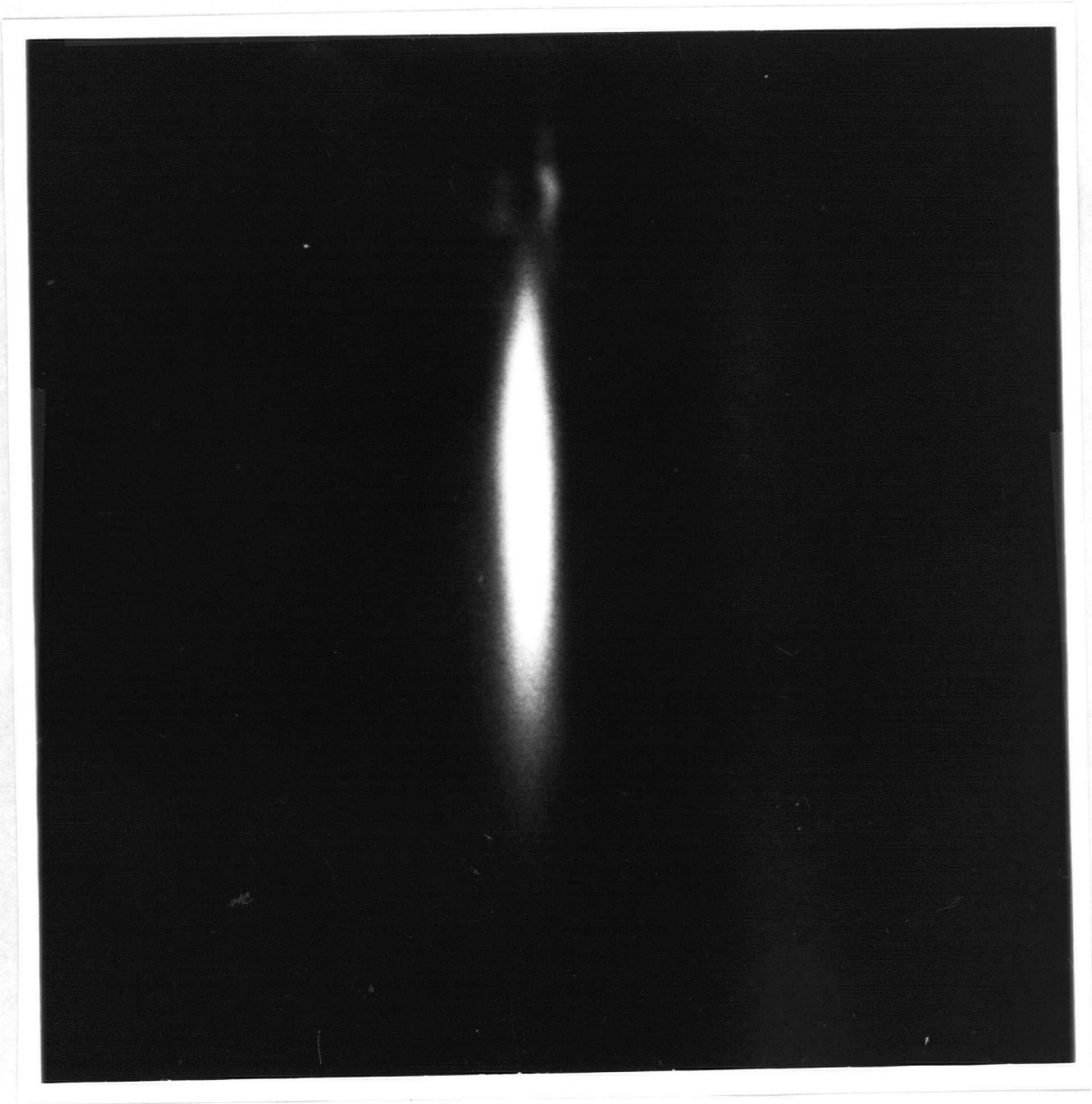

Figure IV-5 Streak photograph of plasma exhaust velocity

(see page 47a)

C) Particle Velocity

Figure IV-6 shows a photograph of the space-time history of an ablatively accelerated foil. This streak photograph has been taken by the insertion of a beam splitter into the oscillator cavity as previously discussed in the last chapter. The photos are reproduceable from shot to shot and from several photographs an average value for the particle velocity has been found to be 2.47×10^5cm/sec.± 10%. This gives us a shock velocity which corresponds to the speed of sound in aluminum.

Figure IV-7 and Figure IV-8 show scanning electron micrograph photos of an irradiated target. Notice the lip of Figure IV-7. These photos show evidence that a force has been created by the absorption of laser energy.

In order to extract all the fluid parameters from the experimental results given in this chapter, an additional set of equations must be added to the shock relations introduced in Chapter II.

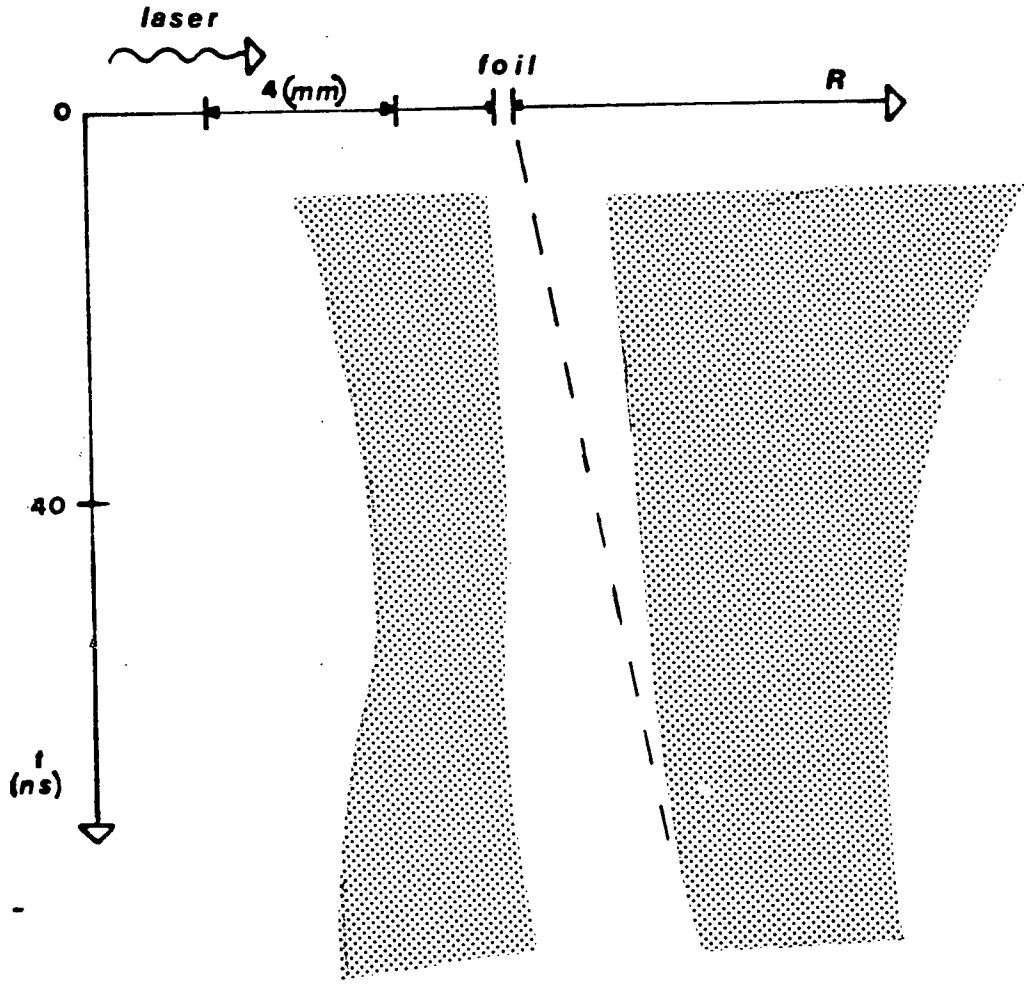

-slope of the dashed line indicates the foil velocity

Figure IV-6 Streak photograph of ablatively accelerated foil

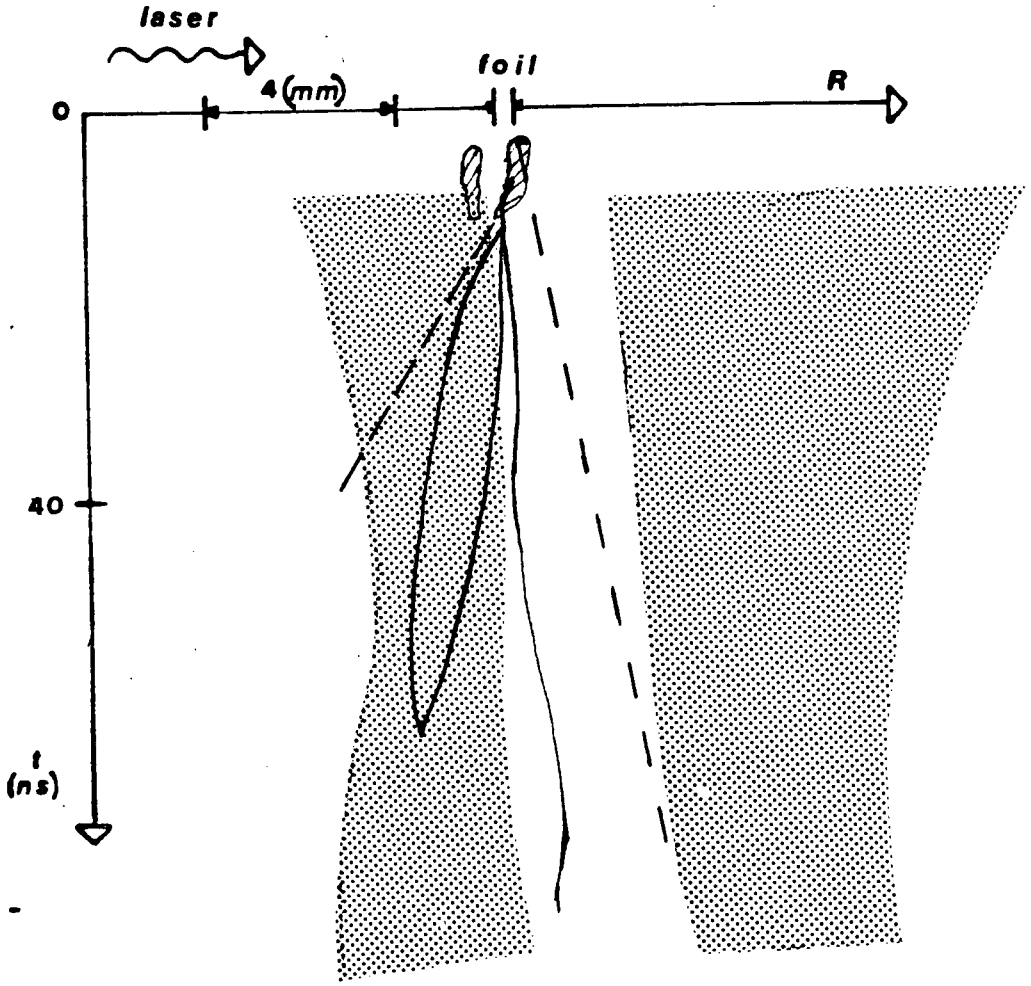

-superposition of the three streak photographs from pages 46a,47a,and49a

Figure IV-7 Electron micrograph side on view of foil

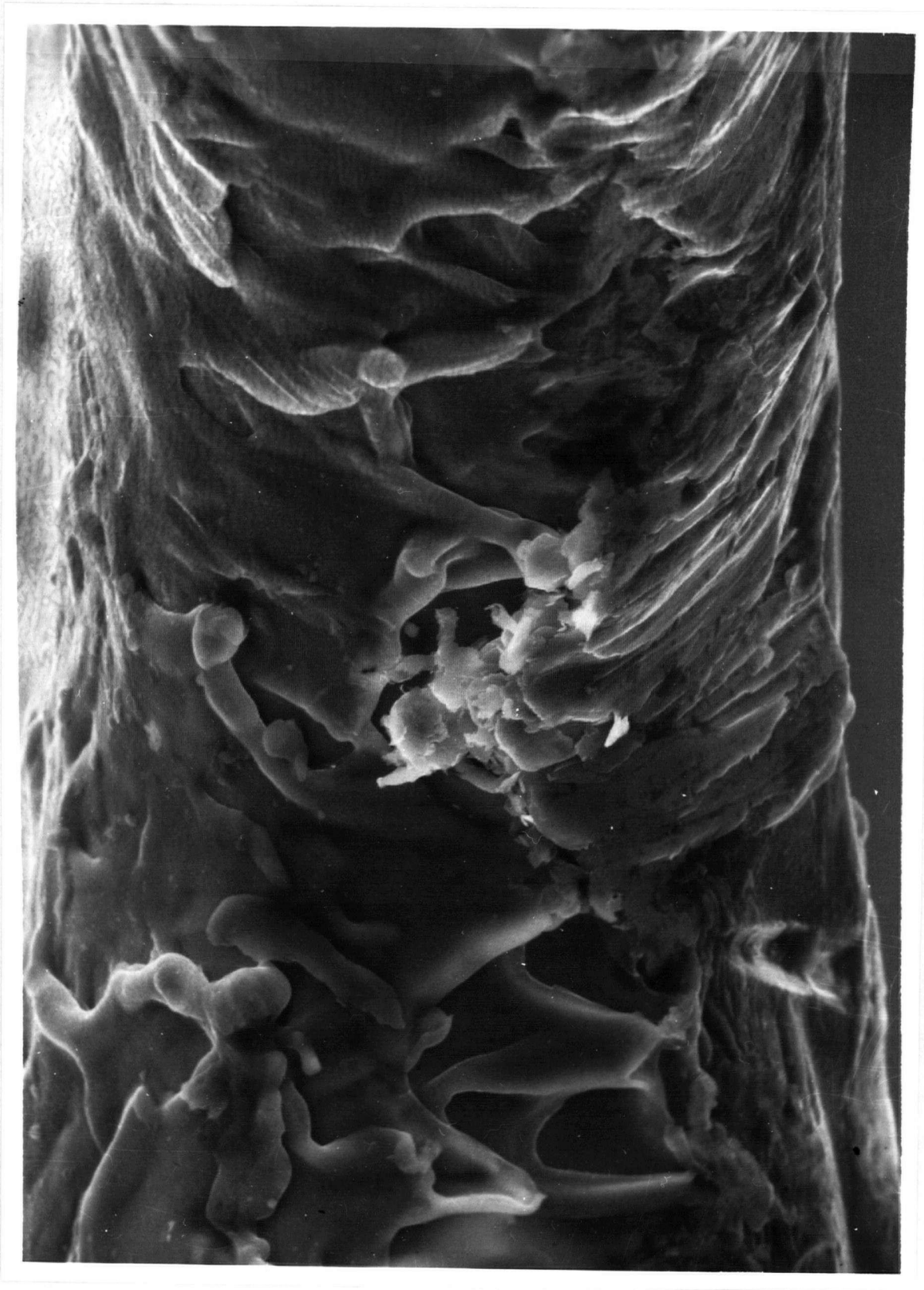

Figure IV-8 Electron micrograph - inner view of foil

CHAPTER V

An Analytical Model for Ablative Pushers

In this chapter an analytical model for a subsonic heat wave which is preceded by a shock wave is developed from a more general heat wave model which considers all possible physical modes (ref. 14). The mode for laser-solid target interactions has been classified by the physics of the situation as follows. The target is an ablative pusher since the electron mean free path and the absorption length are small in comparison to the target thickness. The solid target material is irradiated by the laser pulse from the left as shown in Figure V-1. Initially the laser heats the surface of the material to within a few wavelengths. The region which is heated acts as a heat wave where the expansion wave density is lower on the hot side than on the cool side and therefore is classified as a subsonic heat wave. Furthermore, a shock may propogate into the target ahead of the heat front.

Figure V-1 shows a section of the target when the laser intensity is at peak power. The model considers the fluid parameters in which the local power input I is a constant. The ablation process is considered at the instant of peak compression and a comparison is made with the results of the Medusa hydrocode. The hydrocode is described in the next chapter. Not all of the laser power I is transferred to the ablation front but only a specified fraction $W = \eta I$. In this

model it is assumed that the laser target absorption occurs by the mechanism of inverse bremsstrahlung. This means that the electrons absorb energy from the electric field and collisionally transfer their energy to the ions throughout the whole corona up to the ablation front.

The ablation front is described by the heat wave relations for a discontinuity by the equations of conservation of mass, momentum and energy. In the ablation front's frame of reference the relations are written as:

$$\rho_a v_a = \rho_b v_b \tag{1}$$

$$P_a + \rho_a v_a^2 = P_b + \rho_b v_b^2 \tag{2}$$

$$\frac{1}{2} v_a^2 + h_a + \left(\frac{\rho_a v_a}{W}\right)^{-1} = \frac{1}{2} v_b^2 + h_b \tag{3}$$

where the subscript a refers to quantities ahead of the ablation front and b refers to the quantities behind the ablation front and ρ is the density, p the pressure, v the velocity of the ablation front, v_b the velocity of the plasma plume. In addition, h is the enthalpy which contains the thermodynamics of the material in the numerical value of the enthalpy coefficient g.

Along with the above equations the shock conservation equations (1), (2), and (3) in Chapter II are rewritten here for convenience:

$$\rho_1 v_1 = \rho_2 v_2 \tag{5}$$

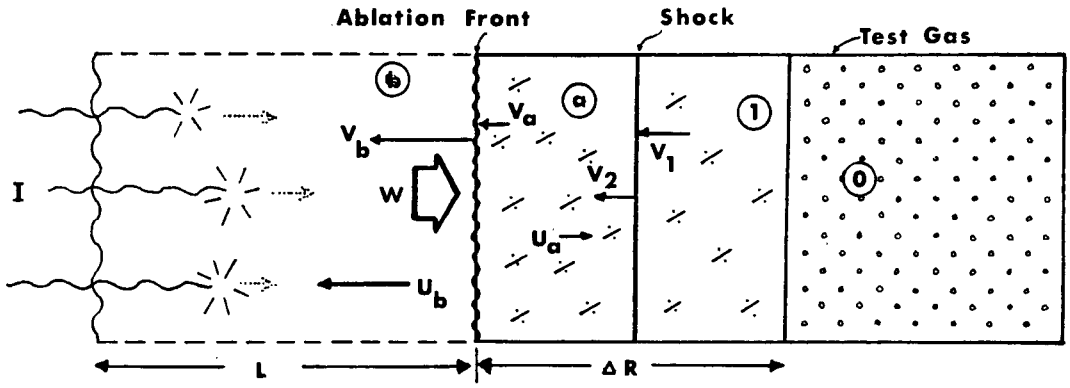

Figure V-1 Section of shell and blowoff plasma

$$p_1 + \rho_1 v_1^2 = p_2 + \rho_2 v_2^2 \tag{6}$$

$$\frac{1}{2} v_1^2 + h_1 = \frac{1}{2} v_2^2 + h_2 \tag{7}$$

$$h_2 = \frac{g_2}{g_2 - 1} \frac{p_2}{\rho_2} \tag{8}$$

and are described as in Chapter II.

Assuming the W is given, the number of unknowns in both sets of equations is twelve:

$$v_a,\ v_b,\ v_1,\ v_2,\ u_a,\ u_b,\ P_a,\ \rho_a,\ h_a,\ P_b,\ \rho_b,\ h_b,$$

but there are only 10 equations, so that one needs to know two more relations to solve this set and predict the plasma parameters.

In addition to the above set of equations the simplified rocket equation

$$u_b v_b \rho_b = u_a (\rho_1 v_1 - \rho_a v_a) \tag{9}$$

can be used, so that only one additional relation is missing. It is therefore possible to express all the unknowns as a function of just one parameter. Here the quantity h_b is chosen as the independent parameter.

By manipulation of the conservation equations the ratios of the pressures, densities and velocities across the heat wave become:

$$\frac{\rho_a}{\rho_b} = \frac{V_b}{V_a} = 1 + \frac{1}{g_a M_a^2} F \tag{10}$$

$$\frac{P_b}{P_a} = 1 - F \tag{11}$$

where

$$F = \frac{g_b - g_a M_a^2}{g_b + 1} \left\{ 1 \pm \sqrt{1 + G - \frac{2 g_a^2 M_a^2 (g_b^2 - 1) W}{(g_a - 1)(g_b - g_a M_a^2)^2 \rho_a V_a h_a}} \right\}$$

and

$$G = \frac{2(g_b + 1)(g_a - g_b) g_a M_a^2}{(g_b - 1)(g_b - g_a M_a^2)^2}$$

which vanishes if either $M_a \gg 1$, $M_b \ll 1$, or $g_a = g_b$.

A useful linear approximation for slow subsonic waves is that the heat input:

$$W \gg \frac{(g_a - 1)(g_b - M_a^2)^2 \rho_a v_a h_a}{2 g_a^2 M_a^2 (g_b^2 - 1)}$$

and then by linear expansions (ref. 21) one finds:

$$\frac{v_b}{v_a} = \frac{\rho_a}{\rho_b} = 1 + \frac{g_a}{g_a - 1} \frac{g_b - 1}{g_b} \left\{ \frac{W}{\rho_a v_a h_a} - \frac{g_a - g_b}{g_a (g_b - 1)} \right\} \tag{12}$$

$$\frac{P_b}{P_a} = 1 - M_a^2 \frac{g_a^2(g_b-1)}{g_b(g_a-1)} \left\{ \frac{W}{\rho_a v_a h_a} - \frac{g_a-g_b}{g_a(g_b-1)} \right\} \tag{13}$$

$$\frac{h_b}{h_a} = 1 + \frac{W}{\rho_a v_a h_a} \approx \frac{\rho_a}{\rho_b} \tag{14}$$

For a subsonic heat wave preceded by a shock the following transformations hold:

$$u_a = v_1 - v_2 \tag{15}$$

$$u_a = v_b - v_a \tag{16}$$

where u is defined positive away from the heat wave (Figure IV-1).

For shock waves W=0 and by manipulation:

$$P_2 = \frac{2\rho_1 v_1^2}{g_2+1} = \frac{2g_2 M_2^2}{(g_2+1)} = \rho_1 v_1 u_2 \tag{19}$$

$$\frac{\rho_2}{\rho_1} = \frac{g_2+1}{g_2-1 + \dfrac{2g_2}{g_2 M_a^2}} \tag{20}$$

$$u_2 = v_1 - v_2 \tag{21}$$

$$h_2 = \frac{2g_2}{(g_2+1)^2} v_1^2 = \frac{g_2}{2} u_2^2 \tag{22}$$

The enthalpy is connected to this set of equations by the equation of state and then there are enough equations to obtain the unknowns in terms of W, ρ_1, h_b . Table I, column (a) shows the result. Often it is more convenient to display these results in graphic form. This can be done by plotting

every parameter as a function of h and W (Fig. V-2).

Now that the general relations for heat waves have been introduced the results can now be applied to the laser-plasma interaction if one additional relation is given. Here we introduce the heating characteristic $h = f[W(I)]$ for inverse bremsstrahlung absorption.

As mentioned previously, the absorbed fraction of the total incident laser intensity I is:

$$W = \eta I \tag{23}$$

The quantity of energy which is absorbed per cm^3 per sec. is I/λ_{ib}. The length λ_{ib} is the absorption length for inverse bremsstrahlung and is given by the standard relation:

$$\lambda_{ib} = 5.83 \times 10^{-37} \frac{\lambda^2 I Z}{T_b^{3_2}} n_{eb}^{\ 2} (cm) \tag{24}$$

where λ is wavelength in microns, I is the laser intensity in watts per cm^2, n_{eb} is the number of particles per cm^3 and T_b is the temperature in the plasma plume.

If we multiply by the length of the corona L, the total absorption per cm^2 becomes:

$$\dot{Q} = IL/\lambda_{ib} \tag{25}$$

At peak compression which is assumed to be in steady state, the power density $\dot{Q}$, absorbed per cm^2 must be used up in the ablation process and therefore it can be set equal to the net power density W. The net heat input W regulates the

temperature and density in the corona which in turn determines the absorption by inverse bremsstrahlung absorption. This absorption model is called self-regulated inverse bremsstrahlung and therefore the ablation and absorption are coupled through the density which is given by:

$$n_{eb} = \frac{\rho_b Z}{m_i} \tag{26}$$

where ρ_b is the density behind of the ablation front Z, is the atomic number and m_i is the mass of an ion.

Substituting for ρ_b from Table I, column (6) into equation (3), the exhaust density becomes:

$$n_{eb} = \frac{\rho_b}{m_i/Z} = \frac{Z}{m_i} \frac{W}{\left(\frac{g_2-1}{g_2}\right)^{1/2} h_b^{3/2}} \tag{27}$$

If the assumption is made that $T_e=T_i$ then the enthalpy becomes:

$$h_b = \frac{Z+1}{m_i} k T_b \tag{28}$$

As stated previously the transferred power W is a fraction of the total incident intensity I at peak compression. Therefore we find that:

$$\frac{IL}{\lambda_{ib}} = \eta I \tag{29}$$

Substituting equations 22, 24, and 27 into 25 one finds:

$$T_b(ev) = 1.2 \times 10^{-3} (LZ)^{2/7} \eta^{2/9} (\lambda I)^{4/9} \tag{30}$$

where L is in microns, Z the atomic number, λ is in microns, and I is in watts per cm^2.

Therefore the heating characteristic for inverse-bremsstrahlung absorption is found from equation 28:

$$h_b = 1.5 \times 10^9 \, \eta^{2/9} (LZ)^{2/7} (I\lambda)^{4/9} \qquad (31)$$

It may be displayed as a line in the response plane, as shown in Fig. V-2.

The parameters L, Z and η are raised to small powers and therefore have little effect on the heating characteristic and hence the results. Setting Z=10 and L=50 um and

$$h_b = 1.5 \times 10^9 \, \eta^{2/9} (I\lambda)^{4/9} .$$

If L is varied by a factor of 10, the numerical constant for the enthalpy changes only by a factor of 1.7 (ref. 14). Therefore the error is about 3. This is illustrated by the "shaded wide" line in Figure IV-3.

Table II, column (b) shows after substitution for h_b the results for ablative flow. Figure V-2 shows the parameters of ablative acceleration as a function of net absorbed power W and the exhaust enthalpy h_b.

It is possible to calculate the kinetic energy generated per unit time in the ablative acceleration process and express it as a function of the absorbed power W. A most important and interesting result is found which shows that

Free flow	(a) 1-D heat wave, cgs units, $g_b = 5/3$	(b) $h_b = 1.5 \times 10^9 \eta^{2/9} (\lambda I)^{4/9}$ (erg/g) I(watt/cm^2); λ(μm); ρ(g/cm^3)
Ablation pressure $p_a \approx p_b$	$0.63 \frac{W}{h_b^{1/2}}$	$1.6 \times 10^{-10} \eta^{8/9} I^{7/9} \lambda^{-2/9}$ (Mbar)
Shocked particle velocity u_2	$0.69 \frac{(W/\rho)^{1/2}}{h_b^{1/4}}$	$11 \times \eta^{4/9} I^{7/18} \lambda^{-1/9} \rho_1^{-1/2}$ (cm/sec)
Burn velocity v_a	$0.25 \frac{W}{\rho_1 h_b}$	$1.7 \times 10^{-3} I^{5/9} \eta^{7/9} \lambda^{-4/9} \rho_1^{-1}$ (cm/sec)
Mass ablation m	W/h_b	$7 \times 10^{-3} \eta^{7/9} I^{5/9} \lambda^{-4/9}$ (g/cm^{2}sec)
Shock energy conversion η	$p_a u_a / W = 0.44 \frac{(W/\rho_1)^{1/2}}{h_b^{3/4}}$	$1.8 \times 10^{-4} \eta^{1/3} I^{1/6} \lambda^{-1/3} \rho_1^{-1/2}$
Exhaust density ρ_b	$W/(0.63\, h_b^{3/2} + 0.25\, W/\rho_1)$	$\approx 2.7 \times 10^{-7} \eta^{2/3} I^{1/3} \lambda^{-2/3}$ (g/cm^3)
Blow off velocity v_b	$0.63\, h_b^{1/2} + W/4\rho_1 h_b$	$\approx 2.4 \times 10^4 \eta^{1/9} I^{2/9} \lambda^{2/9}$ (cm/sec)
Blow off Mach number M_b	$1/g_b^{1/2} \approx 0.8$	≈ 0.8
Absolute exhaust velocity u_b	$0.63 h_b^{1/2} - 0.7 (W/\rho_1)^{1/2} h_b^{-1/4}$	$\approx v_b$

Table I

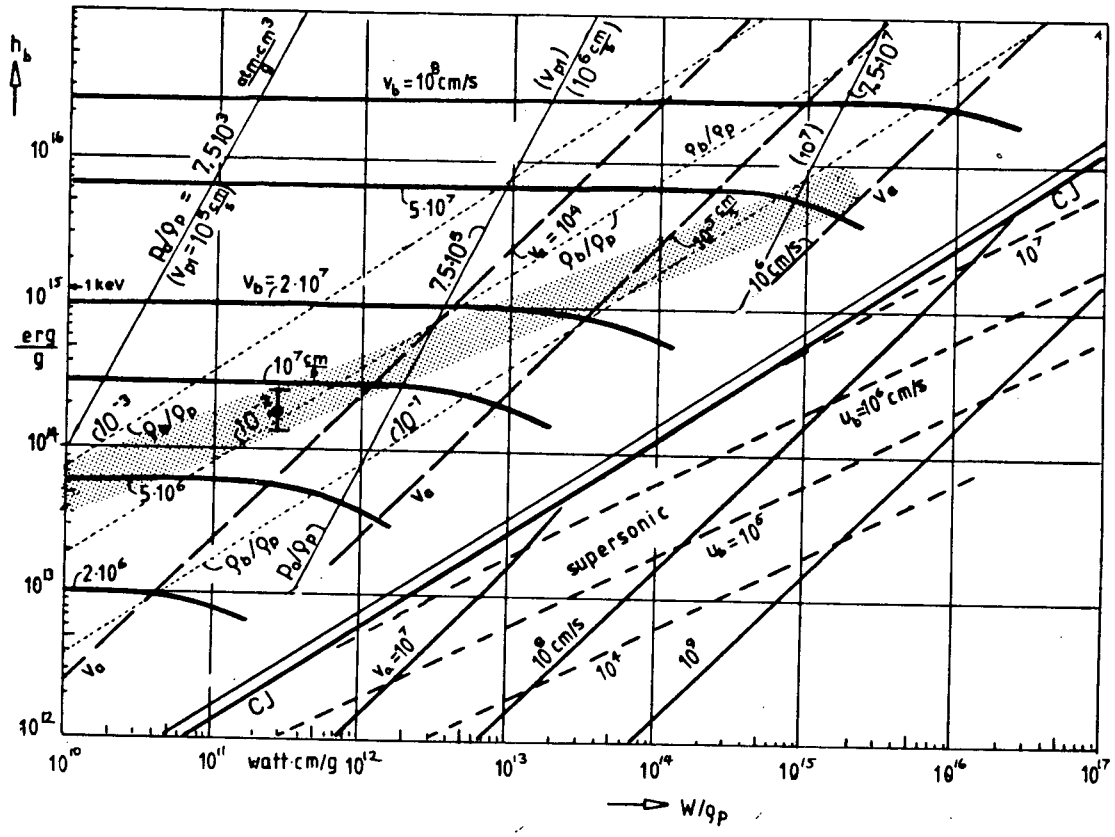

Figure V-2 Parameters of the ablation front as function of net absorbed intensity W and exhaust enthalpy for a flow with rocket type momentum balance. The inverse bremsstrahlung relation is indicated as a shaded wide "line".

the mechanical power $p_a u_a$ can be determined for the ablative mode.

$$n = \frac{\text{mechanical power}}{\text{absorbed heat}} = \frac{g_a - 1}{g_a} = 40\%$$

for $g_a = 5/3$.

The amount of laser energy absorbed by the target is 50%. From the above calculations 40% of the net absorbed energy went into mechanical power while 60% went into the heating of the plasma. Table II summarizes these results in energy units.

Table II

Total Energy	4.0 J
Net absorbed	2.0 J
Mechanical Power	.80J
Plasma Heating	1.20J

In Chapter IV we described the measurement of the net absorbed laser energy and from these measurement a point is located in the response plane. It is immediately seen that the point falls well within the inverse bremsstrahlung

heating characteristic. Furthermore, this point allows the prediction of the "shock" velocities of 3.3×10^5 cm/sec. This predicted value agrees well with the measurements of Chapter IV.

In conclusion, we find that the model which assumes inverse bremsstrahlung absorption agrees well with the experimental findings and indeed demonstrates the existence of a universal heating characteristic. It is interesting to compare these measurements and step wave model calculations with detailed predictions of a hydrocode. Available in this laboratory is the Medusa code, and the next chapter explains how it operates.

CHAPTER VI

The Medusa Hydrocode

A) Brief Description of the Physics of Medusa

The Medusa hydrocode was developed by Christiansen et al. (ref. 13) at the Rutherford Laboratory, England. A version of the Medusa hydrocode has been installed on computer by R.G. Evans (ref. 21). The code describes the motion of a fluid slab which is gradually set in motion when a laser pulse with a given wavelength, beam width, and power is applied onto solid targets.

Initially the assumption is made that the solid target is fully ionized. This is not an unrealistic approximation (ref. 24) since the energy required to ionize an atom is small compared to the energy needed to heat it to some millions of degrees Kelvin. In Medusa calculations the initial stages of plasma production from a solid target are ignored and a fully ionized plasma is assumed to exist with ion and electron densities equal to the solid atom density. In these experiments this density corresponds to solid aluminum. This means that initially the target is not bound together but expands due to the 1eV initial temperature and pressure and forms a corona.

The laser light cannot penetrate into the expanding corona beyond critical density where the plasma frequency is equal to the laser frequency. At the critical density the

absorption is assumed to occur via inverse bremsstrahlung (ref. 1). This means that the laser light decreases exponentially as it penetrates into the expanding plasma, causing the electrons to oscillate in the electric field and collisionally transfer their energy to the ions. This gives the rate of absorption of the laser light. The exchange of energy between electrons and ions is proportional to the electron density and temperature, charge number and the difference between the ion and electron temperatures (ref. 25).

Of course not all of the energy is transferred by collisions to ions and other electrons. Some energy is re-radiated by a process which is termed bremsstrahlung. The mechanism of energy loss is that a free electron abruptly reduces its velocity in the presence of an ion field and the resulting energy appears as a photon. As with inverse bremsstrahlung the rate of energy loss is proportional to the electron density, temperature and charge number of the ion.

The energy transport mechanism between the critical surface and ablation front is a complicated phenomena (ref. 26). At 10^{12} W/cm^2 the heat conduction term in the Medusa code is taken from Spitzer (ref. 26). The important point is that the energy is carried into the plasma and ablates the surface, creating a rocket like thrust which accelerates the target. If the energy transported to the surface is large enough, a shock wave develops which further

compresses and accelerates the foil material.

The rate of absorption, the rate of energy loss to radiation etc., the heat conduction and shock heating are source and sink terms for the conservation of energy. These source and sink terms in the energy equation constitute the conservation of energy. From the conservation of energy a numerical technique is utilized which extracts T_e and T_i.

Once T_e and T_i have been extracted by an iterative procedure the corresponding pressures can be calculated from the perfect gas equations of state. The Navier Stokes equation (ref. 15) is then solved for the plasma velocity which defines the motion. The Medusa code is Lagrangian. This means that a point within the plasma moves with the fluid.

The foil is divided into N cells (mesh) as illustrated in Figure VI-1 for N=7. Note that within the mesh some quantities are defined at cell centres and others at boundaries.

The technique for advancing a particular mesh point is basically understood as follows. The code has five time levels. The old, current and next time levels are represented by 1,3, and 5 respectively. The levels which are in between 1 and 3, and 3 and 5 are denoted by 2 and 4 respectively. For example, let us consider the following quantities $\Delta P1$, $\Delta P3$, $\Delta P5$, $\Delta U2$, $\Delta U4$ where ΔP is the pressure differential and ΔU is the velocity differential.

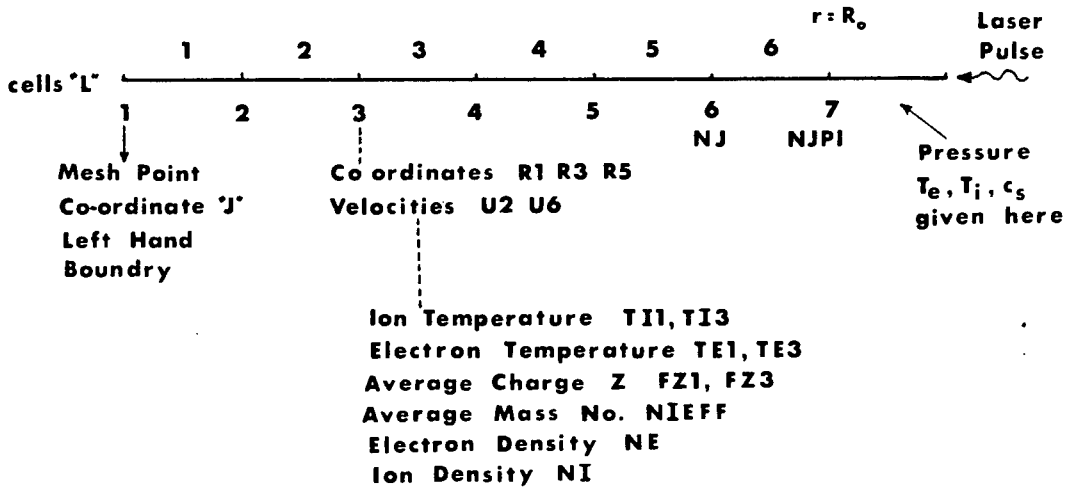

Figure VI-1 Foil divided into a mesh of 6

By knowing the pressure at the old time level $\Delta P1$, the current time level $\Delta P3$ is calculated by solving the energy conservation equation as discussed previously. Some $\Delta U1$ and $\Delta U3$ are known by taking their average $\Delta U2$ is calculated with minimal error. Then since $\Delta U2$ and $\Delta P3$ are known the code extrapolates to calculate $\Delta U4$ until:

$$\frac{\Delta u4 + \Delta u2}{2} = \Delta u3$$

Then $\Delta U4$ advances the position coordinate R3 to the new position R5 since the time Δt between successive advances is known. Section B summarizes the procedure or advancing a mesh point in a do loop flow diagram.

B) The Time Levels in Medusa

Medusa has 5 time levels, e.g.:

R1, R3, R5, U2, U4

where R represents coordinates and U - velocities.

3 is the "current" time level

1 is the "old" time level

5 is the next time level

Basically Medusa loops as follows:

Knowing (R1,R3) and the P, U and T at level 1
solve energy conservation for thermodynamics at level 1 by iteration, then
calculate pressure at level 3, P3
knowing U2 and P3 perform fluid acceleration to give U4
use U4 to advance R3 to R5
copy R3 to R1, R5 to R3, U4 to U1, $(thermo)^3$ to $(thermo)^1$
then laser light is absorbed
return

For details of the equations and numerical techniques refer to Christiansen et al. (ref. 13) and the cited references.

C) User Specifications

To use Medusa, one must specify various parameters which suite a particular experiment. In specifying the physics for most ordinary runs the user must input the laser wavelength, power, pulse shape and duration. The pulse shape can be specified either as triangular or Gaussian. The target material, thickness, and the number of mesh points must also be set before a run. For all normal terms and if it is desired to save on CPU time the perfect gas laws are reasonable in retrospect. For summary and a complete list of variable parameters which may be of use in high intensity simulations, see R.G. Evans (ref. 21).

It has been found that some of the assumptions and applications of the existing code are rather uncertain. The

equation of state is only theoretically inferred and the stability of the compression process is not considered. Furthermore, the code does not treat the absorption region or the physics of the back of the target in full detail.

In the next chapter a comparison is made between experiments and model with the Medusa hydrocode.

CHAPTER VII

Comparison of Analytic Model and Experiments with Medusa

A) Comparison

This chapter compares the experimental and analytic results with the Medusa hydrocode simulations at peak power. The program has been run for a planar aluminum target 37.5um thick, density ρ =2.5 g./cm^3 and ionic charge Z =13. The pulse shape, net power absorbed and wavelength are specified according to the results presented in Chapter IV. Figure VII-1 shows the results for the simulation up to peak compression.

We notice from the simulation that for our laser intensity Medusa does not predict a strong shock wave since the velocity is close to the sound velocity in aluminum. Therefore Medusa implies that our shock wave diagnostic is not applicable to our existing laser system. However one can check if the experimental results and heat wave model are consistent with Medusa calculations. At the present laser intensity, the target is ablatively accelerated in a forward direction like a rocket. From the simulations one extracts the particle velocity (u_2=2.85 x 10^5 cm/sec.), the ablation velocity (v_a=10^4 cm./sec.), the exhaust velocity (v_b =10^7 cm/sec.) and the ablation pressure (P_a =.1 Mbar) (see Fig. VII-1).

Since the amount of net power absorbed has been

measured and the heating characteristic is known all the laser parameters can be determined from the heat wave model from the measurement of the laser intensity alone. Figure V-2 shows the response plane. The point in the plane shows all the laser parameters involved in the ablative flow. As a check two additional parameters were measured as discussed in Chapter III. The exhaust and particle velocities were measured which verifies the heat wave model since it agrees with the model calculations and numerical simulations.

Table III shows the values of the parameters from the experiments and model as compared to those predicted from the Medusa numerical simulation at peak compression. The results suggest very good agreement at the present laser intensity.

Table III

	Experiments	Model	Medusa
W	1.9×10^{11}W-cm/g	1.9×10^{11}W-cm/g	1.9×10^{11}W-cm/g
V_b	9.0×10^{6}cm/sec	8.3×10^{6}cm/sec	1.0×10^{7}cm/sec
U_2	2.47×10^{5}cm/sec	2.3×10^{5}cm/sec	2.85×10^{5}cm/sec
V_a	-	5.0×10^{3}cm/sec	7.5×10^{3}cm/sec
P_a	-	.1Mbar	.1Mbar

Figure VII-2 shows the ablation temperature as a function of

laser intensity. The circles represent experimental values from other laboratories (ref. 27). The square represents the exhaust temperature for the existing laser facility.

These results verify a universal heating characteristic for laser produced plasmas from which the exhaust temperature can be predicted from the measurement of the laser intensity alone.

B) Future Work

In order to test the validity of the analytical model developed in Chapter II, it would be of great interest and of value to irradiate laser targets with a higher intensity. From the response plane (Fig. V-2) strong shocks start at a laser intensity of 10^{14} W/cm^2. A CO2 laser system capable of producing such high intensities is operational at University of British Columbia.

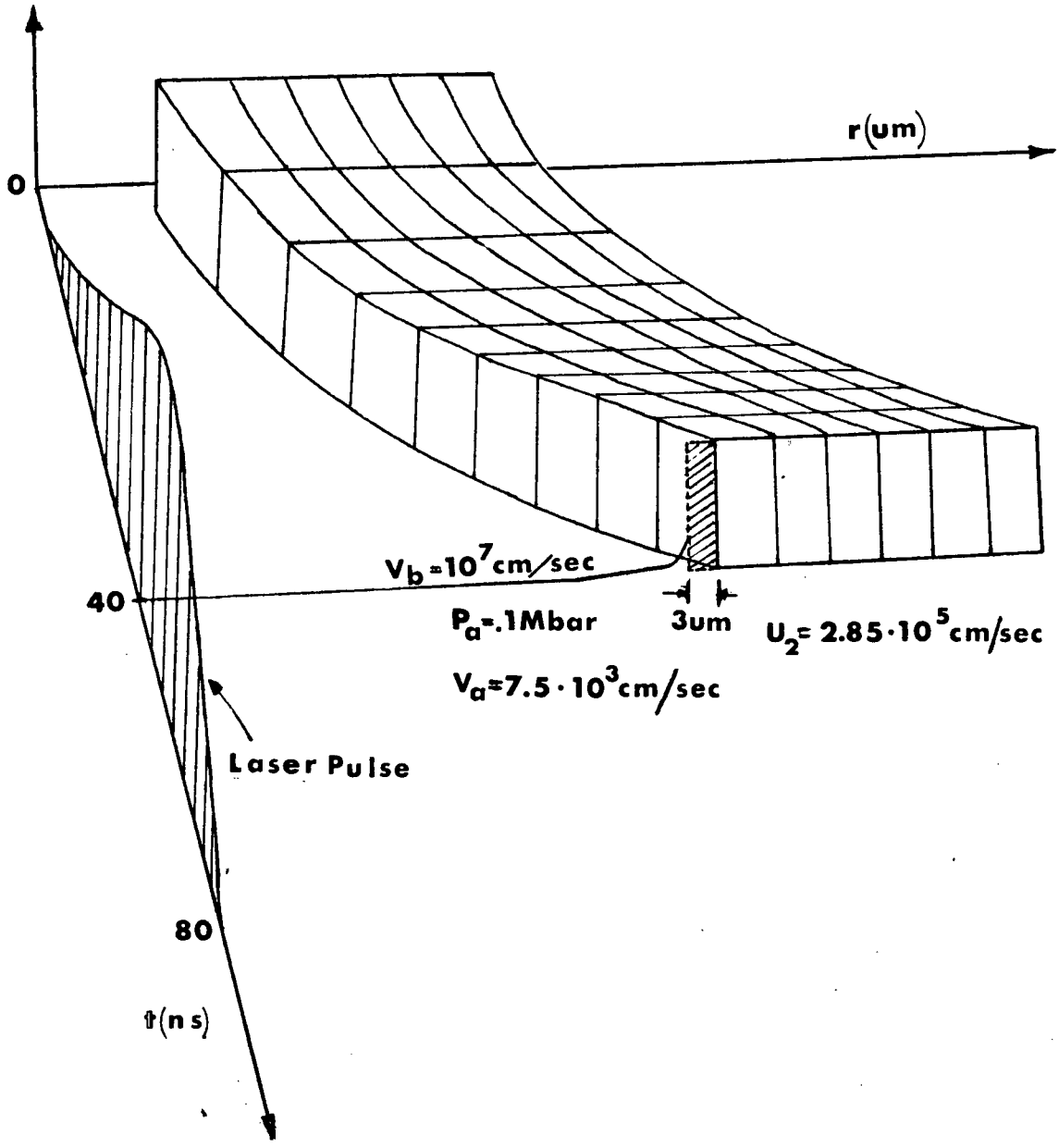

Figure VII-1 Medusa simulation up to peak compression

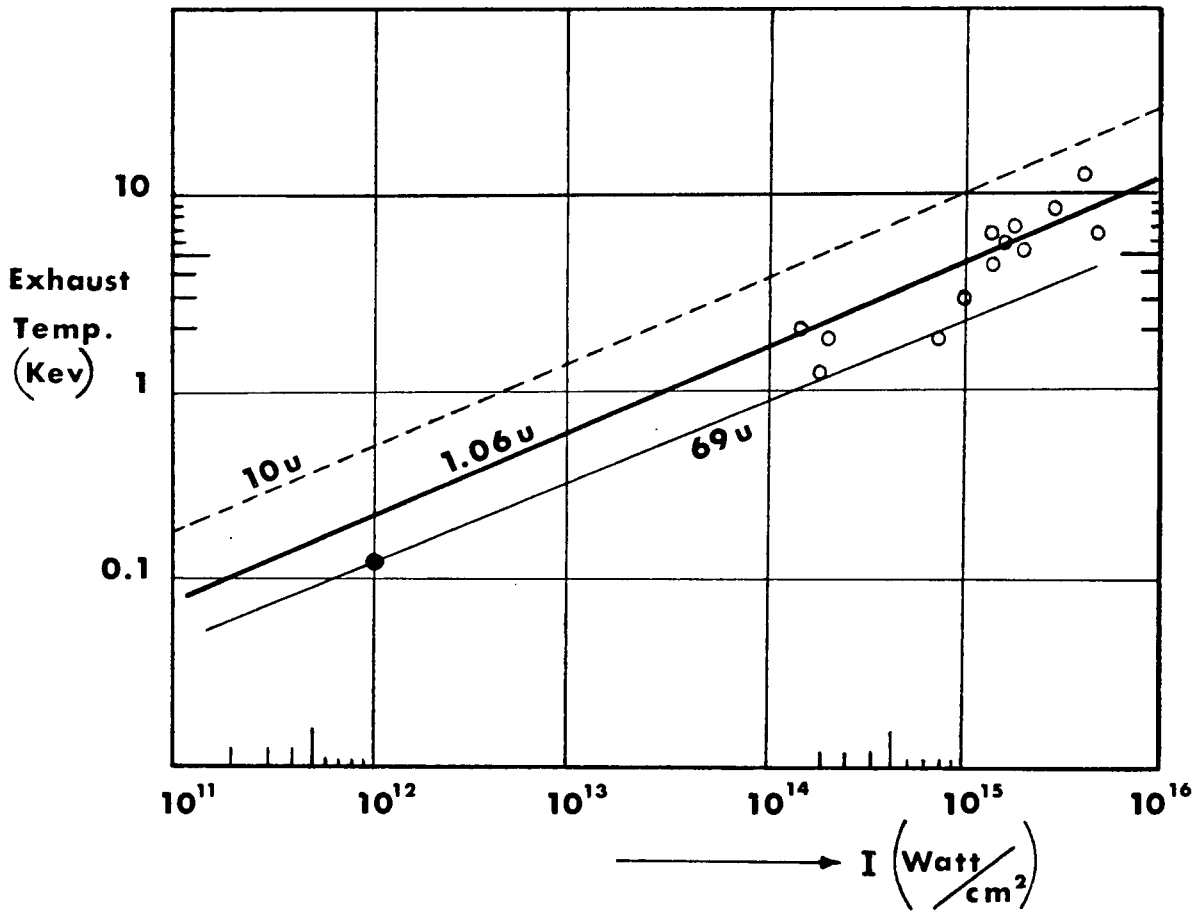

Figure VII-2 Ablation temperature as a function of laser intensity and experimental values of ref. 27

REFERENCES

1 L.D. Vessor and J.C. Solem, Phys. Rev. Lett. 40, 1391 (1978)

2 R.J. Trainor, J.W. Shaner, J.M. Auerbach, and N.C. Holmes, Phys. Rev. Lett. 42, 1154 (1979)

3 L.R. Vessor, J.C. Solem, and A.J. Leiber, Appl. Phys. Lett. 35, 761 (1979)

4 B. Arad, S. Fliezer, Y. Gazit, H.M. Loebenstein, A. Zigler, H. Szmora, and S. Zweigenbaum, J. App. Phys. 50, 6817 (1979)

5 M.H. Key, Nature 283, 715 (1980)

6 N.H. Burnett, G. Josin, B. Ahlborn, and R. Evans, Appl. Phys. Lett. 38(4) Feb. 15, 1981.

7 Albach, G. M.Sc. Thesis. University of British Columbia 1972

8 Godfrey, L.A. M.Sc. Thesis. University of British Columbia 1972

9 Churchland, M., M.Sc. Thesis. University of British Columbia 1969

10 Hilko, B. M.Sc. Thesis. University of British Columbia 1978

11 TRW Model ID Image Converter Camera, Technical Manual.

12 B. Ahlborn, G. Josin, A. Ng, and N.H. Burnett, Paper #5R75, Bull. Am. Phys. Soc. 25 933 (1980)

13 J.P. Christiansen et al., Computer Phys. Comm. 7 (1974) 278-287.

14 B. Ahlborn, M. Keg, Rutherford Lab report RL-79-033

15 N.H. Burnett, G. Josin, B. Ahlborn and R. Evans to be published (1980).

16 Samson, Physics in Canada (CAP Meeting, Quebec) 32, No. 3, 12 (1976).

17 B.H. Ripin et al. ICP '80 topical meeting on inertial confinement fusion, San Diego Feb. 26-28 (1980) paper WB 3.

18 B. Ahlborn, Can. J. Physics (1975), 53, 976.

19 B. Ahlborn, IPP Report III/12 Garching (1963).

20 Ashby, Christiansen, and Roberts Computer Physics Communications Vol. 7, No. 5, p. 271 (1974).

21 R.G. Evans, U.B.C. Lab Report Number 75

22 W.I. Lintor, Appl. Phys. Lett. 3, 210 (1963).

23 W. Demtriode, and W. Jantz, Plasma Physics, Vol. 12, pp. 691-705.

24 Hughes, Plasmas and Laser Light, Alan Hilger

25 D.J. Rose and M. Clarke, Plasmas and Controlled Fusion (John Wiley, Inc., 1961)

26 L. Spitzer, Physics of Fully Ionized Gases, 2nd ed. (Interscience Pub., 1961)

27 P.T. Rumsby, M. Michaelis, M. Burgess (1975) Opt. Comm. 15, 242.